View metadata, citation and similar papers at core.ac.uk
brought to you by CORE
provided by RERO DOC Digital Library

Microscopic gauge-invariant theory of the *c*-axis infrared response of bilayer cuprate superconductors and the origin of the superconductivity-induced absorption bands

Jiří Chaloupka,[1,*] Christian Bernhard,[2] and Dominik Munzar[1]
[1]*Department of Condensed Matter Physics, Faculty of Science, Masaryk University, Kotlářská 2, 61137 Brno, Czech Republic*
[2]*Department of Physics and Fribourg Center for Nanomaterials, Chemin du Musée 3, CH-1700 Fribourg, Switzerland*

We report on results of our theoretical study of the *c*-axis infrared conductivity of bilayer high-T_c cuprate superconductors using a microscopic model involving the bilayer-split (bonding and antibonding) bands. An emphasis is on the gauge invariance of the theory, which turns out to be essential for the physical understanding of the electrodynamics of these compounds. The description of the optical response involves local (intrabilayer and interbilayer) current densities and local conductivities. The local conductivities are obtained using a microscopic theory, where the quasiparticles of the two bands are coupled to spin fluctuations. The coupling leads to superconductivity and is described at the level of generalized Eliashberg theory. Also addressed is the simpler case of quasiparticles coupled by a separable and nonretarded interaction. The gauge invariance of the theory is achieved by including a suitable class of vertex corrections. The resulting response of the model is studied in detail and an interpretation of two superconductivity-induced peaks in the experimental data of the real part of the *c*-axis conductivity is proposed. The peak around 400 cm^{-1} is attributed to a collective mode of the intrabilayer regions, which is an analog of the Bogolyubov-Anderson mode playing a crucial role in the theory of the longitudinal response of superconductors. For small values of the bilayer splitting, its nature is similar to that of the transverse plasmon of the phenomenological Josephson superlattice model. The peak around 1000 cm^{-1} is interpreted as a pair-breaking feature that is related to the electronic coupling through the spacing layers separating the bilayers.

http://doc.rero.ch

I. INTRODUCTION

The *c*-axis infrared response of the high-T_c cuprate superconductors (HTCSs) is strongly sensitive to doping.[1–3] For underdoped HTCS, it reveals a surprisingly weak coupling between adjacent unit cells[4] and a pronounced pseudogap (PG).[5] In optimally doped materials, the real part of the normal-state (NS) conductivity σ_c is almost frequency and temperature independent for a broad range of frequencies and temperatures.[3] In contrast, the response of overdoped HTCS exhibits a metallic behavior.[3] These findings, in particular the pseudogap, and the qualitative nature of the changes across the phase diagram, make the *c*-axis response one of the most interesting properties of the HTCS (for a review see Ref. 6). In materials with two copper-oxygen planes per unit cell (the so-called bilayer compounds), the *c*-axis response also reflects the electronic coupling within the pair of closely spaced planes, which is of high interest for the following reasons: (i) Its renormalization with respect to the noninteracting case is an important fingerprint of the electronic correlations of the ground state. (ii) For underdoped HTCS, the manifestations of the pseudogap in σ_c interfere with those of the coupling. A prerequisite for an understanding of the *c*-axis pseudogap is, thus, a disentanglement of the former from the latter. (iii) The coupling may contribute to the condensation energy (see Refs. 7 and 8 and references therein).

The character of the coupling has been debated since the early years of the high-T_c research. According to the conventional band theory, the hopping between the planes should lead to a splitting of the conduction band into two branches: a bonding branch corresponding to states that are symmetric with respect to the mirror plane in the middle of the bilayer unit, and an antibonding branch corresponding to states that are antisymmetric.[9] For some regions of the Brillouin zone (BZ), the bonding band is expected to be located below the Fermi level and the antibonding band above, which should give rise to the interband transitions.[10]

The experimental NS infrared spectra of the bilayer compounds, however, do not contain any structure that could be easily attributed to the transitions. Furthermore, the 20th-century photoemission experiments did not reveal the splitting of the conduction band. These findings could be interpreted in terms of strong electronic correlations localizing charged quasiparticles in individual planes, even in the case of the bilayer unit, and inhibiting the band splitting. The simple band-structure-based picture of the NS, thus, seemed to have failed. The experimental superconducting (SC)-state infrared spectra of underdoped bilayer compounds exhibit features that are almost certainly related to the bilayer coupling: a broad absorption peak in the spectra of Re σ_c in the frequency region between 350 cm^{-1} and 550 cm^{-1} (labeled as P_1 in the following), and related anomalies of some infrared-active phonons.[1,2,11] These features, however, also appear to be consistent with the absence of the conduction-band splitting and the localization of charged quasiparticles: It was shown that they can be well understood and in some cases even fitted[11,12] using the phenomenological model, where the stack of the copper-oxygen planes is represented by a superlattice of interbilayer and intrabilayer Josephson junctions [the so-called Josephson superlattice model (JSM)].[13] The mode P_1 has been attributed to the transverse plasma mode of the model. A microscopic justification of the

http://doc.rero.ch

model in terms of quasiparticle Green's functions has been provided by Shah and Millis.[14]

In the beginning of the 21st century, the situation changed. In particular, several groups have reported observations of two separate conduction bands in photoemission spectra.[15–19] The JSM is obviously not consistent with this observation. In addition, it became clear that the SC-state spectra of Re σ_c of $YBa_2Cu_3O_{7-\delta}$ (Y-123) exhibit two distinct superconductivity-induced modes: the mode P_1 discussed above and another one around 1000 cm^{-1} (to be labeled as P_2).[8,20] It has been proposed that the two are related, but in the light of the results of the recent systematic study by Yu *et al.*[20] this appears to be unlikely. The presence of P_2 cannot be accounted for in terms of the JSM. These facts, thus, call for a replacement of the simple phenomenological JSM with a more sophisticated theory involving the bilayer-split bands. Here we present such a theory and provide a fully microscopic interpretation of the superconductivity-induced modes P_1 and P_2.

The basic ingredients of the theory are: (i) The local current densities, conductivities, fields, and a generalized multilayer formula. The local current densities of the intrabilayer and interbilayer regions are expressed in terms of local conductivities and local fields. The fields differ from the average field because of charge fluctuations between the planes. Macroscopic considerations of these charging effects lead to a formula for the total c-axis conductivity, which represents an extension of the common multilayer formula.[13] (ii) The local conductivities are calculated using a microscopic model and the linear-response theory. This is the main difference with respect to the phenomenological JSM, where they are estimated or obtained by fitting the data. (iii) The microscopic description involves the two bilayer-split bands. The relevance of the bilayer splitting to the interpretation of the c-axis response has been pointed out in Ref. 21. (iv) The charged quasiparticles of the two bands are coupled to spin fluctuations. The coupling is treated at the level of generalized Eliashberg theory, as in Ref. 22. (v) The gauge invariance of the theory, required for a consistent, i.e., charge conserving description of the charging effects, has been achieved by including a class of vertex corrections (VC) ensuring that the renormalized current vertices satisfy the appropriate Ward identities. The vertex corrections will be shown to lead to dramatic and qualitative changes in the calculated response, similar to those occurring in case of the longitudinal response of a homogeneous superconductor.

Calculated spectra of Re σ_c allow us to understand the nature of the peaks P_1 and P_2. The former will be shown to correspond to a collective mode resembling the Bogolyubov-Anderson mode of homogeneous superconductors and the latter to a pair-breaking (bonding-antibonding) peak.

The rest of the paper is organized as follows. In Sec. II we present the essential aspects of the theory, the values of the input parameters, and some computational details. Section III contains results and discussion. In Sec. III A we focus on the relatively simple case of a Bardeen-Cooper-Schrieffer (BCS)-like interaction between the quasiparticles. The analysis allows one to understand the consequences of the bilayer splitting and the role of the vertex corrections, but the resulting spectra of Re σ_c are not sufficiently realistic. The complex case of quasiparticles coupled to spin fluctuations is addressed in Sec. III B. It will be shown that the calculated SC-state spectra display two distinct modes, similar to the experimental ones. Section III C presents a comprehensive discussion of the relation between theory and experiment including the interpretation of the superconductivity-induced modes. The summary and conclusions are given in Sec. IV. The readers interested only in the main findings of the paper may consider skipping Sec. II, and some technical parts of Secs. III A and III B.

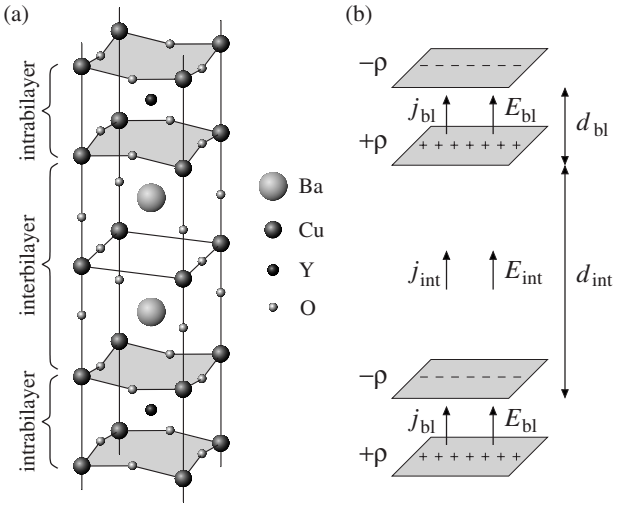

FIG. 1. (a) Crystal structure of Y-123. (b) Multilayer model, where intrabilayer and interbilayer current densities j_{bl} and j_{int} lead to a charge redistribution between the CuO_2 planes, which modifies the local fields E_{bl} and E_{int}.

II. THEORY

In this section we elaborate on the basic ingredients of our theory mentioned in Sec. I. First we briefly describe a phenomenological approach to the c-axis electrodynamics of the bilayer systems. In the subsequent paragraphs, we build up a corresponding microscopic description.

A. Multilayer model

The multilayer model proposed by van der Marel and Tsvetkov[13] provides a phenomenological description of the c-axis electrodynamics of bilayer cuprates. These compounds are considered as consisting of homogeneously charged copper-oxygen planes separated by intrabilayer (bl) and interbilayer (int) spacing regions (see Fig. 1). The dielectric function of the intrabilayer region,

$$\varepsilon_{bl}(\omega) = \varepsilon_\infty + \frac{i\sigma_{bl}(\omega)}{\varepsilon_0\omega}, \tag{1}$$

contains the interband dielectric constant ε_∞ and the local conductivity σ_{bl} defined by $j_{bl}=\sigma_{bl}E_{bl}$, where j_{bl} is the local current density and E_{bl} is the local field. The interbilayer region is described in a similar way using the local conductivity σ_{int}. To obtain the macroscopic (total) c-axis dielectric function $\varepsilon(\omega)$, modifications of the local fields due to the

charging of the planes have to be considered. The result is

$$\frac{d}{\varepsilon(\omega)} = \frac{d_{\rm bl}}{\varepsilon_{\rm bl}(\omega)} + \frac{d_{\rm int}}{\varepsilon_{\rm int}(\omega)}. \quad (2)$$

An extended version of the model that we use in this paper includes the dependence of the local current densities on both local fields,

$$j_L = \sum_{L'} \sigma_{LL'} E_{L'}, \quad L,L' \in \{\rm bl, int\}. \quad (3)$$

The total c-axis conductivity $\sigma_c(\omega)$ is given as the ratio of the average current density $\langle j\rangle = (d_{\rm bl} j_{\rm bl} + d_{\rm int} j_{\rm int})/d$ to the average electric field $\langle E\rangle = (d_{\rm bl} E_{\rm bl} + d_{\rm int} E_{\rm int})/d$. By employing the continuity relation between the charge and current densities $j_{\rm int} - j_{\rm bl} = \partial\rho/\partial t$ and the effect of the charged planes on the local fields, $E_{\rm bl} - E_{\rm int} = \rho/\varepsilon_0\varepsilon_\infty$ (see Fig. 1), we arrive at

$$\sigma_c(\omega) = \frac{d_{\rm bl}\sigma_{\rm bl/bl} + d_{\rm int}\sigma_{\rm int/bl}}{d_{\rm bl} + d_{\rm int}\alpha} + \frac{d_{\rm bl}\sigma_{\rm bl/int} + d_{\rm int}\sigma_{\rm int/int}}{d_{\rm bl}\alpha^{-1} + d_{\rm int}}, \quad (4)$$

where

$$\alpha = \frac{E_{\rm int}}{E_{\rm bl}} = \frac{\sigma_\infty + \sigma_{\rm bl/bl} - \sigma_{\rm int/bl}}{\sigma_\infty + \sigma_{\rm int/int} - \sigma_{\rm bl/int}} \quad (5)$$

and $\sigma_\infty = -i\omega\varepsilon_0\varepsilon_\infty$. The total dielectric function is given by $\varepsilon(\omega) = \varepsilon_\infty + i\sigma_c(\omega)/\varepsilon_0\omega$.

In the following we describe the calculations of the local conductivities $\sigma_{LL'}$ based on a microscopic model. The subsequent incorporation of the interplane Coulomb interaction will then provide a microscopic justification for the phenomenological treatment of the plane-charging effects used in the model of van der Marel and Tsvetkov.

B. Electronic structure—tight-binding bands, their renormalization, and superconductivity

One of the main components of our microscopic calculations is the two bilayer-split bands. We, therefore, begin with the tight-binding description of these bands. The usual form of the in-plane dispersion

$$\epsilon_{\boldsymbol{k}_\parallel} = -2t(\cos k_x a + \cos k_y a) - 4t' \cos k_x a \cos k_y a \quad (6)$$

will be considered, with the nearest-neighbor and second-nearest-neighbor hopping matrix elements t and t'. The intrabilayer hopping is governed by the hopping matrix element $t_{\perp\boldsymbol{k}_\parallel}$ that is assumed to depend on k_x and k_y as

$$t_{\perp\boldsymbol{k}_\parallel} = \frac{t_{\perp\,\rm max}}{4}(\cos k_x a - \cos k_y a)^2. \quad (7)$$

This approximate form is suggested by the results of local-density approximation (LDA) calculations[9] and is roughly consistent with experimental data on $Bi_2Sr_2CaCu_2O_{8+\delta}$ (Bi-2212).[16] Let us note that the essential results of our calculations do not depend on the form of $t_{\perp\boldsymbol{k}_\parallel}$, what matters is the magnitude. In addition to the intrabilayer hopping, we consider a weak coupling through the interbilayer region with the matrix element $t'_{\perp\boldsymbol{k}_\parallel}$ of the same $\boldsymbol{k}$ dependence as $t_{\perp\boldsymbol{k}_\parallel}$. The interlayer hopping splits band (6) into two bands—bonding (B) and antibonding (A)—with the dispersions

$$\epsilon_{B/A\boldsymbol{k}} = \epsilon_{\boldsymbol{k}_\parallel} \mp \sqrt{t^2_{\perp\boldsymbol{k}_\parallel} + t'^2_{\perp\boldsymbol{k}_\parallel} + 2t_{\perp\boldsymbol{k}_\parallel} t'_{\perp\boldsymbol{k}_\parallel} \cos k_z d}. \quad (8)$$

To account for the renormalization of charged quasiparticles and the superconducting pairing we adopt the spin-fermion model, where the quasiparticles are coupled to spin fluctuations. In the case of a single band, the model self-energy (2 by 2 matrix) is given by

$$\Sigma(\boldsymbol{k}, i\!E) = \frac{g^2}{\beta N}\sum_{\boldsymbol{k}', i\!E'} \chi_{\rm SF}(\boldsymbol{k}-\boldsymbol{k}', i\!E - i\!E')\mathcal{G}(\boldsymbol{k}', i\!E'), \quad (9)$$

which can be schematically written as the convolution $\Sigma = g^2\chi_{\rm SF} \star \mathcal{G}$. Here g is the coupling constant, $\chi_{\rm SF}$ is the Matsubara counterpart of the spin susceptibility, and $\mathcal{G}$ the Nambu propagator, $\mathcal{G}(\boldsymbol{k}, i\!E) = [i\!E\tau_0 - (\varepsilon_{\boldsymbol{k}} - \mu)\tau_3 - \Sigma(\boldsymbol{k}, i\!E)]^{-1}$.

The generalization to the two band case is straightforward and the self-energies can be expressed as[23,24]

$$\Sigma_{B/A} = g^2\chi^{\rm odd}_{\rm SF} \star \mathcal{G}_{A/B} + g^2\chi^{\rm even}_{\rm SF} \star \mathcal{G}_{B/A}, \quad (10)$$

where we distinguish between the spin-susceptibility channels of even ($\chi^{\rm even}_{\rm SF}$) and odd ($\chi^{\rm odd}_{\rm SF}$) symmetry with respect to the mirror plane in the center of the bilayer unit. The diagrammatic representation of $\Sigma_{B/A}$ is shown in Fig. 2(a). We have used the same form of $\chi_{\rm SF}$ containing the resonance mode and a broad continuum as in Ref. 22 (details will be given in Sec. II F). The spin susceptibility consisting of the mode and a continuum has been successfully used by Eschrig and Norman[25] to explain various aspects of the charged quasiparticles in the high-T_c cuprates (for a review, see Ref. 26).

Since the results of the self-consistent calculations based on the spin-fermion model are difficult to interpret, we first resort to the BCS level. The results obtained this way are easier to understand because of the absence of retardation and better possibilities of analytical manipulations of the formulas. The even- and odd-interaction channels are assumed to be equivalent, which leads to the same superconducting gap $\Delta_{\boldsymbol{k}} = \frac{1}{2}\Delta_{\rm max}(\cos k_x a - \cos k_y a)$ in both bands determined by

$$\Delta_{\boldsymbol{k}} = -\sum_{\boldsymbol{k}', n\in\{A,B\}} V_{\boldsymbol{k}\boldsymbol{k}'} \frac{\Delta_{\boldsymbol{k}'}}{2E_{\boldsymbol{k}'n}} \tanh\frac{\beta E_{\boldsymbol{k}'n}}{2}, \quad (11)$$

where $V_{\boldsymbol{k}\boldsymbol{k}'} = -\lambda w_{\boldsymbol{k}} w_{\boldsymbol{k}'}$ with $w_{\boldsymbol{k}} = (\cos k_x a - \cos k_y a)/2$ is the BCS interaction of d-wave symmetry and $E_{\boldsymbol{k}A/B}$ is the usual BCS quasiparticle energy $E_{\boldsymbol{k}A/B} = \sqrt{(\epsilon_{\boldsymbol{k}A/B} - \mu)^2 + \Delta^2_{\boldsymbol{k}}}$. For details see the Appendix.

C. Response to electromagnetic field

Here we calculate the response of the model to the c-axis polarized electromagnetic field represented by the external vector potential $\boldsymbol{A}_{\rm ext} = (0,0,A_{\rm ext})e^{i\boldsymbol{q}\cdot\boldsymbol{R} - i\omega t}$. The coupling of the tight-binding model to the electromagnetic field can be obtained by multiplying each hopping term by the corresponding Peierls phase factor according to the prescription[27–29] $c^\dagger_{\boldsymbol{R}} c_{\boldsymbol{R}'} \to \exp[-(ie/\hbar)\boldsymbol{A}_{\rm ext}\cdot(\boldsymbol{R}-\boldsymbol{R}')]c^\dagger_{\boldsymbol{R}} c_{\boldsymbol{R}'}$. To fit the scheme of

http://doc.rero.ch

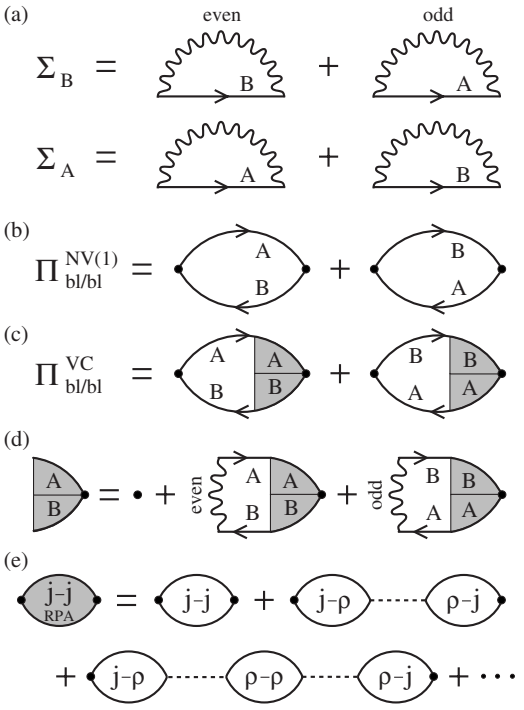

FIG. 2. (a) Diagrammatic representation of the self-energies of the bonding (B) and antibonding (A) bands. The propagators of the electronic quasiparticles and spin fluctuations are represented by the straight and the wiggly lines, respectively. (b) Simple bubble approximation to current-current correlator (20). Only the part given by Eq. (21) is shown. The black dots are the current vertices corresponding to $j^p_{\rm bl}$. (c) Current-current correlator with a renormalized current vertex [Eq. (23)]. The diagrams corresponding to the case of $t'_{\perp k_\parallel}=0$ with no intraband contributions are shown. (d) Diagrammatic representation of the Bethe-Salpeter Eq. (24). (e) Diagrammatic representation of the equation determining the current-current correlator including plane-charging effects. The dashed lines correspond to the interplane Coulomb interaction.

Sec. II A, we formally distinguish between the vector potentials $A_{\rm bl}$ and $A_{\rm int}$, used for the hopping processes through the intrabilayer and interbilayer regions, respectively. By expanding to the second order in the vector potentials, we arrive at the coupling Hamiltonian that can be used for extracting the c-axis paramagnetic and diamagnetic current-density operators.[27] The paramagnetic current density for $\boldsymbol{q}=0$, averaged over the corresponding region (bl/int), can be expressed as

$$\hat{J}^p_{\rm bl/int}=-\frac{ie}{Na^2\hbar}\sum_{\boldsymbol{k}_\parallel k_z s}\left[\pm J^{(1)}_{\rm bl/int,\boldsymbol{k}}(c^\dagger_{Aks}c_{Bks}-c^\dagger_{Bks}c_{Aks})\right.$$
$$\left.+J^{(2)}_{\boldsymbol{k}}(c^\dagger_{Aks}c_{Aks}-c^\dagger_{Bks}c_{Bks})\right] \tag{12}$$

with the matrix elements

$$J^{(1)}_{{\rm bl},\boldsymbol{k}}=\frac{2t_{\perp\boldsymbol{k}_\parallel}(t_{\perp\boldsymbol{k}_\parallel}+t'_{\perp\boldsymbol{k}_\parallel}\cos k_z d)}{\epsilon_{A\boldsymbol{k}}-\epsilon_{B\boldsymbol{k}}} \tag{13}$$

and

$$J^{(2)}_{\boldsymbol{k}}=\frac{2it_{\perp\boldsymbol{k}_\parallel}t'_{\perp\boldsymbol{k}_\parallel}\sin k_z d}{\epsilon_{A\boldsymbol{k}}-\epsilon_{B\boldsymbol{k}}}. \tag{14}$$

The matrix element $J^{(1)}_{{\rm int},\boldsymbol{k}}$ is obtained from $J^{(1)}_{{\rm bl},\boldsymbol{k}}$ simply by interchanging $t_{\perp\boldsymbol{k}_\parallel}$ and $t'_{\perp\boldsymbol{k}_\parallel}$. In the $t'_{\perp\boldsymbol{k}_\parallel}=0$ case, where $J^{(1)}_{{\rm bl},\boldsymbol{k}}=t_{\perp\boldsymbol{k}_\parallel}$ and $J^{(1)}_{{\rm int},\boldsymbol{k}}=J^{(2)}_{\boldsymbol{k}}=0$, we arrive at the simplified expression

$$\hat{J}^p_{\rm bl}=-\frac{ie}{N_\parallel a^2\hbar}\sum_{\boldsymbol{k}_\parallel s}t_{\perp\boldsymbol{k}_\parallel}(c^\dagger_{A\boldsymbol{k}_\parallel s}c_{B\boldsymbol{k}_\parallel s}-c^\dagger_{B\boldsymbol{k}_\parallel s}c_{A\boldsymbol{k}_\parallel s}). \tag{15}$$

The summation runs over $\boldsymbol{k}_\parallel$ from the two-dimensional (2D) Brillouin zone only and N is reduced accordingly. The diamagnetic current density is given by

$$\hat{J}^d_{\rm bl/int}=-\frac{e^2 d_{\rm bl/int}A_{\rm bl/int}}{Na^2\hbar^2}\sum_{\boldsymbol{k}_\parallel k_z s}\left[J^{(1)}_{{\rm bl/int},\boldsymbol{k}}(n_{Bks}-n_{Aks})\right.$$
$$\left.\mp J^{(2)}_{\boldsymbol{k}}(c^\dagger_{Aks}c_{Bks}-c^\dagger_{Bks}c_{Aks})\right]. \tag{16}$$

In the $t'_{\perp\boldsymbol{k}_\parallel}=0$ case, Eq. (16) simplifies to

$$\hat{J}^d_{\rm bl}=-\frac{e^2 d_{\rm bl}A_{\rm bl}}{N_\parallel a^2\hbar^2}\sum_{\boldsymbol{k}_\parallel s}t_{\perp\boldsymbol{k}_\parallel}(n_{Bks}-n_{Aks}). \tag{17}$$

The total c-axis conductivity is constructed along the lines of Sec. II A. To this end, the current densities induced by the electric fields $E_L=i(\omega+i\delta)A_L(L\in\{{\rm bl},{\rm int}\})$ have to be calculated and the local conductivities determined from $j_L(\boldsymbol{q},\omega)=\Sigma_{L'}\sigma_{LL'}(\boldsymbol{q},\omega)E_{L'}(\boldsymbol{q},\omega)$. At this point, the fields $E_{L'}$ are still equal to the *external* field $E_{\rm ext}$. However, it will be shown in Sec. II E that the local conductivities calculated as outlined above, ignoring the charging effects play exactly the same role as in Eq. (3), i.e., they represent the response to the *local* fields. Within the framework of the linear-response theory, the local conductivities are given by the Kubo formula

$$\sigma_{LL'}(\boldsymbol{q},\omega)=\frac{(e^2/\hbar^2)K_L\delta_{LL'}+\Pi_{LL'}(\boldsymbol{q},\omega)}{i(\omega+i\delta)}. \tag{18}$$

The first term in the numerator,

$$K_{\rm bl/int}=-\frac{d_{\rm bl/int}}{Na^2}\sum_{\boldsymbol{k}_\parallel k_z s}J^{(1)}_{{\rm bl/int},\boldsymbol{k}}\langle n_{Bks}-n_{Aks}\rangle, \tag{19}$$

comes from the diamagnetic current densities and is related to the c-axis kinetic energy:[27] In the $t'_{\perp\boldsymbol{k}_\parallel}=0$ case, $K_{\rm bl}=(d_{\rm bl}/a^2)\langle T\rangle$, where $\langle T\rangle$ is the intrabilayer kinetic energy per unit cell,

$$T=-(1/N_\parallel)\textstyle\sum_{\boldsymbol{k}_\parallel s}t_{\perp\boldsymbol{k}_\parallel}(n_{B\boldsymbol{k}_\parallel s}-n_{A\boldsymbol{k}_\parallel s})$$
$$=-(1/N_\parallel)\textstyle\sum_{\boldsymbol{R}_\parallel\boldsymbol{R}'_\parallel s}t_{\perp\boldsymbol{R}_\parallel\boldsymbol{R}'_\parallel}(c^\dagger_{2\boldsymbol{R}_\parallel s}c_{1\boldsymbol{R}'_\parallel s}+c^\dagger_{1\boldsymbol{R}_\parallel s}c_{2\boldsymbol{R}'_\parallel s}).$$

The second term in Eq. (18) is the retarded correlation function of the paramagnetic current densities

$$\Pi_{LL'}(\boldsymbol{q},\omega)=i\frac{Na^2d_{L'}}{\hbar}\int_{-\infty}^{\infty}{\rm d}t e^{i\omega t}\langle[\hat{J}^p_L(\boldsymbol{q},t),\hat{J}^p_{L'}(-\boldsymbol{q},0)]\rangle\theta(t). \tag{20}$$

http://doc.rero.ch

http://doc.rero.ch

In the simplest approximation, the correlator is obtained by evaluating the bubble diagrams where the two current vertices are joined by two electron propagator lines. This is the approximation, where the vertex corrections are neglected. Since the propagators refer to the two bands, there are four possible combinations in total. Two of them correspond to interband transitions and their contribution to the Matsubara counterpart of Eq. (20) at $\boldsymbol{q}=0$ equals

$$\Pi^{\mathrm{NV}(1)}_{LL'}(\boldsymbol{q}=0,i\hbar\nu) = \mp\frac{e^2}{\hbar^2}\frac{d_{L'}}{Na^2\beta}\sum_{\boldsymbol{k},iE} J^{(1)}_{L,\boldsymbol{k}}J^{(1)}_{L',\boldsymbol{k}}\mathrm{Tr}[\mathcal{G}_A(\boldsymbol{k},iE+i\hbar\nu) \times\mathcal{G}_B(\boldsymbol{k},iE)+\mathcal{G}_B(\boldsymbol{k},iE+i\hbar\nu)\mathcal{G}_A(\boldsymbol{k},iE)] \quad (21)$$

with the minus sign for $L=L'$ and plus sign for $L\neq L'$. The corresponding diagrams are presented in Fig. 2(b). For $t'_{\perp\boldsymbol{k}_\parallel}\neq 0$, all the conductivity components acquire, in addition, an intraband contribution given by

$$\Pi^{\mathrm{NV}(2)}_{LL'}(\boldsymbol{q}=0,i\hbar\nu) = -\frac{e^2}{\hbar^2}\frac{d_{L'}}{Na^2\beta}\sum_{\boldsymbol{k},iE} J^{(2)}_{\boldsymbol{k}}J^{(2)}_{\boldsymbol{k}}\mathrm{Tr}[\mathcal{G}_A(\boldsymbol{k},iE+i\hbar\nu) \times\mathcal{G}_A(\boldsymbol{k},iE)+\mathcal{G}_B(\boldsymbol{k},iE+i\hbar\nu)\mathcal{G}_B(\boldsymbol{k},iE)]. \quad (22)$$

This contribution has a similar frequency dependence as the in-plane conductivity, the main difference coming from the $\boldsymbol{k}$ dependence of the matrix element $J^{(2)}_{\boldsymbol{k}}$. Typically, it is rather small compared to Eq. (21).

D. Vertex corrections

The well-known deficiency of the simple bubble approximations such as the one leading to Eqs. (21) and (22) is the lack of the gauge invariance which manifests itself, e.g., by a violation of the normal-state restricted sum rule for the conductivity. For the normal state the conductivity components should satisfy the sum rule $\int_{0+}^{\infty}\mathrm{Re}\,\sigma_{LL}(\omega)\mathrm{d}\omega=-(\pi e^2/2\hbar^2)K_L$. While the discrepancy between the left-hand side and the right-hand side in the corresponding case of the in-plane response is rather small [of the order of 1% (Ref. 22)], here it is quite detrimental—typically 20%–30%—as demonstrated in Sec. III. Since there is an intimate relation between the gauge invariance of the response functions and the charge conservation, the large discrepancy indicates that the continuity equation between the current and charge densities is not even approximately satisfied. As a consequence, the use of the formula (4), which relies on the continuity equation, becomes questionable. In the following paragraph we show explicitly how the requirement of gauge invariance enters a microscopic derivation of the formulas of Sec. II A.

To avoid the problems mentioned above, a gauge-invariant extension of the approximation (21)+(22) is necessary. As found by Nambu,[30] the gauge invariance of the response function is guaranteed if we replace the bare current-density vertex with a properly renormalized one. The required renormalization of this vertex (i.e., of the interaction of the quasiparticles with photons) is determined by the form of the quasiparticle self-energy via the generalized Ward identity.[31]

Here the situation is complicated by the presence of the two bands. To be able to express all the contributions in a systematical way, we first introduce the bare vertex factors $(ie/Na^2\hbar)\gamma^L_{nm}(\boldsymbol{k})$ (with $m,n\in\{A,B\}$) inferred from Eq. (12). In the corresponding diagram, the mth band propagator line with momentum $\boldsymbol{k}$ enters the current vertex of j^p_L and the nth band propagator line leaves it. The possible combinations are: $\gamma^{\mathrm{bl}}_{AB}=-\gamma^{\mathrm{bl}}_{BA}=J^{(1)}_{\mathrm{bl},\boldsymbol{k}}$, $\gamma^{\mathrm{int}}_{BA}=-\gamma^{\mathrm{int}}_{AB}=J^{(1)}_{\mathrm{int},\boldsymbol{k}}$, and $\gamma^{\mathrm{bl}}_{BB}=-\gamma^{\mathrm{bl}}_{AA}=\gamma^{\mathrm{int}}_{BB}=-\gamma^{\mathrm{int}}_{AA}=J^{(2)}_{\boldsymbol{k}}$. The correlator $\Pi_{LL'}$ involving the renormalized current vertices $\Gamma^L_{nm}(\boldsymbol{k},iE,i\hbar\nu)$

$$\Pi^{\mathrm{VC}}_{LL'}(\boldsymbol{q}=0,i\hbar\nu) = \frac{e^2}{\hbar^2}\frac{d_{L'}}{Na^2\beta}\sum_{\boldsymbol{k},iE,mn\in\{A,B\}}\mathrm{Tr}[\gamma^{L'}_{mn}(\boldsymbol{k})\mathcal{G}_m(\boldsymbol{k},iE) \times\Gamma^L_{nm}(\boldsymbol{k},iE,i\hbar\nu)\mathcal{G}_n(\boldsymbol{k},iE+i\hbar\nu)] \quad (23)$$

contains two interband contributions with $mn=AB$ and $mn=BA$. The corresponding diagrams are shown in Fig. 2(c). For $t'_{\perp\boldsymbol{k}_\parallel}=0$, these are the only contributions. In the $t'_{\perp\boldsymbol{k}_\parallel}\neq 0$ case, also the intraband terms with $mn=AA$ and $mn=BB$ contribute.

The renormalized vertices $\Gamma^L_{nm}(\boldsymbol{k},iE,i\hbar\nu)$ consistent with the electronic self-energies of the two bands obey the Bethe-Salpeter equations of the form diagrammatically shown in Fig. 2(d). At this point, we have to distinguish between the spin-fluctuation-mediated interaction and the BCS interaction, allowing for further analytical simplifications. Evaluating the diagrams in the former case we arrive at

$$\Gamma^L_{AB}(\boldsymbol{k},iE,i\hbar\nu)=\gamma^L_{AB}(\boldsymbol{k})\tau_0+\frac{g^2}{\beta N}\sum_{\boldsymbol{k}',iE'}\chi^{\mathrm{even}}_{\mathrm{SF}}(\boldsymbol{k}-\boldsymbol{k}',iE-iE') \times\mathcal{G}_B(\boldsymbol{k}',iE')\Gamma^L_{AB}(\boldsymbol{k}',iE',i\hbar\nu)\mathcal{G}_A(\boldsymbol{k}',iE'+i\hbar\nu) +\frac{g^2}{\beta N}\sum_{\boldsymbol{k}',iE'}\chi^{\mathrm{odd}}_{\mathrm{SF}}(\boldsymbol{k}-\boldsymbol{k}',iE-iE') \times\mathcal{G}_A(\boldsymbol{k}',iE')\Gamma^L_{BA}(\boldsymbol{k}',iE',i\hbar\nu)\mathcal{G}_B(\boldsymbol{k}',iE'+i\hbar\nu) \quad (24)$$

and similar equations for the other renormalized vertices. Intraband current vertices Γ^L_{AA} and Γ^L_{BB} turn out to be simply the bare ones because of the symmetry of $\gamma^L_{AA}(\boldsymbol{k})$ and $\gamma^L_{BB}(\boldsymbol{k})$ (odd functions of $\boldsymbol{k}_z$), and q_z independence of $\chi_{\mathrm{SF}}(\boldsymbol{q},\omega)$ assumed in the $t'_{\perp\boldsymbol{k}_\parallel}\neq 0$ case. In the BCS case, the interaction is nonretarded and separable, which leads to a simple $\boldsymbol{k}$ dependence and iE independence of Γ: $\Gamma^L_{AB}(\boldsymbol{k},i\hbar\nu)=\gamma^L_{AB}(\boldsymbol{k})+\lambda w_{\boldsymbol{k}}C^L(i\hbar\nu)$. Here λ is the BCS coupling constant and $w_{\boldsymbol{k}}$ is the d-wave symmetry function introduced in Sec. II B. The Bethe-Salpeter equations and the current-current correlators can then be treated to a large extent analytically,[31] as shown in the Appendix. In addition, the intraband contributions are exactly zero in the optical limit of $\boldsymbol{q}\to 0$.

http://doc.rero.ch

E. Random phase approximation of plane-charging effects

In Sec. II A, we presented the results of a phenomenological approach to the effects due to the charging of the planes. Here we outline a rigorous microscopic derivation of Eq. (2), where these effects are treated at the level of the random-phase approximation (RPA). For the sake of simplicity, we restrict ourselves to the case of insulating interbilayer regions.

The current density within a bilayer unit leads to a redistribution of charge among the CuO_2 planes. The electrostatic interaction of the corresponding charge densities is given by the interaction Hamiltonian

$$\hat{H}_{\mathrm{Coulomb}} = \frac{Na^2 d_{\mathrm{bl}}}{2\varepsilon_\infty \varepsilon_0} \hat{\rho}\hat{\rho}, \tag{25}$$

where $\hat{\rho}$ is the excess planar charge density. The current-current correlator $\Pi_{\mathrm{bl/bl}}$ modified by this interaction along the lines of the RPA approximation, corresponding to the diagrammatic series shown in Fig. 2(e), reads

$$\Pi^{\mathrm{RPA}}_{\mathrm{bl/bl}} = \Pi^{j-j} - \Pi^{j-\rho} \frac{1}{\varepsilon_\infty \varepsilon_0 + \Pi^{\rho-\rho}} \Pi^{\rho-j}, \tag{26}$$

where $\Pi^{j-j} \equiv \Pi_{\mathrm{bl/bl}}$, $\Pi^{j-\rho}$, $\Pi^{\rho-j}$, and $\Pi^{\rho-\rho}$ are the correlation functions obtained without considering the charging effects. To proceed further toward Eq. (2), we have to express these correlation functions using the conductivity-related current-current correlator Π^{j-j} only, eliminating $\Pi^{j-\rho}$, $\Pi^{\rho-j}$, and $\Pi^{\rho-\rho}$. This can be achieved using the continuity equation for the charge and current densities. Let us note that the gauge invariance of the local response functions is the necessary condition for the continuity equation to be valid. The result of the elimination can be written as

$$\sigma^{\mathrm{RPA}}_{\mathrm{bl/bl}} = \frac{\sigma_{\mathrm{bl/bl}}}{1 + \frac{i\sigma_{\mathrm{bl/bl}}}{\varepsilon_\infty \varepsilon_0 \omega}}. \tag{27}$$

The last step is the incorporation of the macroscopic averaging to obtain the macroscopic c-axis dielectric function

$$\varepsilon(\omega) = \varepsilon_\infty + \frac{i}{\varepsilon_0 \omega} \frac{\langle j \rangle}{\langle E \rangle}, \tag{28}$$

where the symbols $\langle j \rangle$ and $\langle E \rangle$ denote the unit-cell averages of the current density and the electric field, respectively. The averaged current density is given by $\langle j \rangle = (d_{\mathrm{bl}}/d) j_{\mathrm{bl}}$ since the interbilayer regions are supposed not to contribute. The macroscopic field $\langle E \rangle$ consists of the homogeneous external field and the averaged field of the induced charge density $\langle E \rangle = E_{\mathrm{ext}} + (d_{\mathrm{bl}}/d)\rho/\varepsilon_0\varepsilon_\infty$. Using the relation $j_{\mathrm{bl}} = \sigma^{\mathrm{RPA}}_{\mathrm{bl/bl}} E_{\mathrm{ext}}$ and the continuity equation $i\omega\rho = j_{\mathrm{bl}}$, we obtain

$$\langle j \rangle = \frac{d_{\mathrm{bl}}}{d} \sigma^{\mathrm{RPA}}_{\mathrm{bl/bl}} E_{\mathrm{ext}}, \quad \langle E \rangle = E_{\mathrm{ext}} - \frac{d_{\mathrm{bl}}}{d} \frac{i\sigma^{\mathrm{RPA}}_{\mathrm{bl/bl}}}{\varepsilon_\infty \varepsilon_0 \omega} E_{\mathrm{ext}}. \tag{29}$$

Finally, by inserting these results in Eq. (28), we arrive at Eq. (2) with $\varepsilon_{\mathrm{int}} = \varepsilon_\infty$ and $\varepsilon_{\mathrm{bl}} = \varepsilon_\infty + i\sigma_{\mathrm{bl/bl}}/\varepsilon_0\omega$. The local response function $\sigma_{\mathrm{bl/bl}}$ calculated in Secs. II C and II D plays the role of σ_{bl}. In the more general case of Eq. (4), the derivation is analogous to the one presented here. We stress that the use of Eq. (2) and (4) is now accompanied by the requirement of the gauge invariance of the local conductivities.

F. Input parameters and computational details

The values of most of the input parameters are the same as in Ref. 22. For the description of the bands we use the in-plane dispersion with $t = 350$ meV, $t' = -100$ meV and the band filling $n = 0.82$. The values of the interplane hopping parameters will be specified later at the corresponding places in the text since various regimes of the optical response corresponding to various values of these parameters are discussed. In the multilayer formula, we use $d_{\mathrm{bl}} = 3.4$ Å, $d_{\mathrm{int}} = 12.0$ Å, i.e., the values corresponding to Bi-2212, and $\varepsilon_\infty = 5$.

The model spin susceptibility has the same form as in Refs. 32 and 22, containing the 40 meV resonance mode and a continuum with dimensionless spectral weights of $0.01 b_M$ and $0.01 b_C$, respectively. In the $t'_{\perp \boldsymbol{k}_\parallel} = 0$ case, we distinguish between the channels of odd and even symmetry and include the resonant mode with $b_M = 1$ in the odd channel only. The continuum with $b_C = 2$ is present in both channels. For $t'_{\perp \boldsymbol{k}_\parallel} \neq 0$, the bonding and antibonding states are no more of the simple form $|B\rangle, |A\rangle = (|1\rangle \pm |2\rangle)/\sqrt{2}$, where $|1\rangle$ and $|2\rangle$ are state vectors residing on the first and the second plane of the bilayer unit, respectively. The linear combination now contains $\boldsymbol{k}$-dependent coefficients. A proper construction of the interaction vertices would extensively complicate the theory. To avoid this complexity, we take $b_M = 1/2$ and $b_C = 2$ for both channels whenever $t'_{\perp \boldsymbol{k}_\parallel} > 0$.

The coupling constant $g = 3$ eV was chosen to yield T_c around 90 K and the amplitude of the superconducting gap Δ around 30 meV. Some of the calculations were performed on the simpler BCS level, where we choose the value of the BCS coupling constant λ leading to the same gap amplitude of 30 meV.

The self-consistent equations for the self-energies [Eq. (10)] and Bethe-Salpeter [Eqs. (24)] were solved iteratively using a Brillouin-zone grid of typically $64 \times 64 \times 32$ points, and a cutoff of 8 eV in Matsubara frequencies. In the case of small $t_{\perp\,\max} \lesssim 50$ meV, the vertex corrections lead to a complete change in the response-function profiles and up to 10^3 iterations of the Bethe-Salpeter equation are required to achieve the convergence. The convolutions were performed using the fast Fourier transform (FFT) algorithm with the use of the symmetries of Σ and Γ. Since the calculations are very demanding in terms of computer time and memory, we have used q_z-independent spin susceptibility which brings the advantage of k_z-independent Σ and $\Gamma - \gamma$. The calculated response functions were continued to the real axis using the method of Padé approximants.[33]

III. RESULTS AND DISCUSSION

A. Quasiparticles paired by the BCS interaction

We begin with the simpler case of insulating spacing layers, i.e., $t'_\perp = 0$. Figure 3(a) shows the local dielectric function $\varepsilon_{\mathrm{bl/bl}}$ of the intrabilayer region obtained using the bubble diagram of Fig. 2(b), i.e., with the vertex corrections neglected (this is abbreviated as NV). The thin (thick) lines correspond

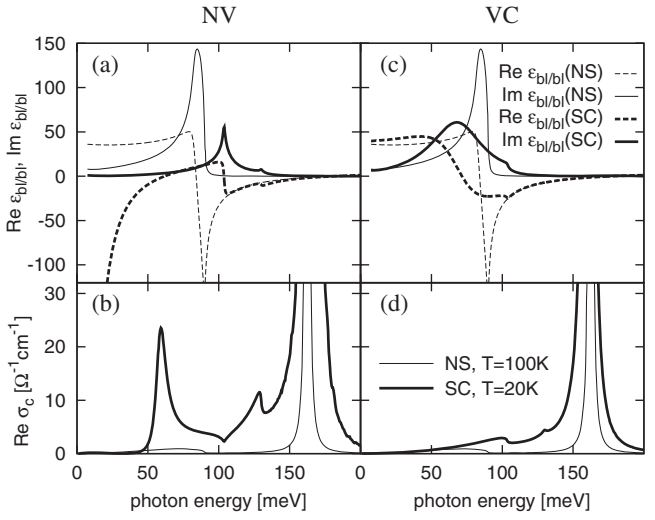

FIG. 3. (a) Local dielectric function $\varepsilon_{bl/bl}$ in the simplest BCS case with $t'_{\perp \boldsymbol{k}_\parallel}=0$, $t_{\perp\,\max}=45$ meV, and $\Delta_{\max}=30$ meV, vertex corrections are not included (NV). The thin (thick) lines correspond to the normal (superconducting) state, $T=100$ K ($T=20$ K). The solid (dashed) lines represent the imaginary (real) part. (b) The real part of the corresponding total c-axis conductivity obtained using Eq. (2). The thin (thick) line corresponds to the normal (superconducting) state. [(c) and (d)] The same as in (a) and (b) but with the VC included (for the superconducting state only).

to the normal (superconducting) state and the solid (dashed) lines represent the imaginary (real) part. The NS response exhibits a sharp absorption band near 80 meV due to the interband (bonding-antibonding) transitions. The SC-state response involves the superconducting condensate, which manifests itself in the real part of $\varepsilon_{bl/bl}$ and a pair-breaking peak at 110 meV, corresponding to final states with one Bogolyubov quasiparticle in the bonding band and one in the antibonding.

Figure 3(b) shows the real part σ_c of the c-axis conductivity obtained using the multilayer formula (2) with $\varepsilon_{bl}=\varepsilon_{bl/bl}$ and $\varepsilon_{int}=\varepsilon_\infty$. The dominant sharp peaks are located close to the frequencies of the zero crossings of $\varepsilon_{bl/bl}$. This can be understood using the fact that for $|d_{bl}\varepsilon_{int}| \ll |d_{int}\varepsilon_{bl}|$ Eq. (2) yields

$$\varepsilon(\omega) \approx \frac{d\varepsilon_{int}}{d_{int}}\left(1-\frac{d_{bl}\varepsilon_{int}}{d_{int}\varepsilon_{bl}}\right) \tag{30}$$

and the expression on the right-hand side has poles at the zero crossings of Re ε_{bl}. Physically, the response is similar to that of a system of thin metallic plates embedded in an insulating matrix, exhibiting a peak at the plasma frequency of the plates (the corresponding effective-medium formulas can be found in Ref. 34). The narrow peak at 160 meV of the NS spectra corresponds to the zero crossing of Re ε_{bl} associated with the interband transitions, the peak of the SC-state spectrum at 60 meV to the zero crossing due to the superconducting condensate.

The VC change the response functions dramatically: the SC-state spectrum of $\varepsilon_{bl/bl}$ shown in Fig. 3(c) displays neither the superconducting condensate nor the pronounced pair-breaking peak. They are replaced by a broad band centered at 70 meV. The real part of $\varepsilon_{bl/bl}$ exhibits only two zero crossings (instead of the three occurring in the NV case, the difference is due to the absence of the condensate). The one at lower energies is located in a region of strong absorption. As a consequence, the SC-state spectrum of σ_c shown in Fig. 3(d) displays only one pronounced maximum located at the same energy as that of the NS.

Below we demonstrate that the absence of the condensate in $\varepsilon_{bl/bl}$ (VC) is a general consequence of the gauge invariance. The current density in the bilayer region induced by a homogeneous electric field $\boldsymbol{E}$ oriented along the c-axis can be expressed employing two different gauges of the electromagnetic potentials:

(a) $\Delta\varphi=0$, $E_c=i\omega A_c$. Here E_c is the c-axis component of $\boldsymbol{E}$, $\Delta\varphi$ is the scalar-potential difference between the two planes, and A_c is the c-axis component of the vector potential;

(b) $A_c=0$, $E_c=-\Delta\varphi/d_{bl}$.

Both approaches should lead to the same result. In the latter case the expression for the conductivity contains only a regular component proportional to a current-density correlator.[31,35] The conductivity, thus, cannot possess a singular component corresponding to the condensate. Note that the above arguments utilizing the two gauges parallel those used when discussing the response of a homogeneous superconductor to a longitudinal probe.

The analogy can be further used to understand the nature of the peak (mode) at 70 meV in Fig. 3(c). We recall that in homogeneous superconductors a longitudinal electromagnetic field excites the Bogolyubov-Anderson (B. A.) mode corresponding to density fluctuations of the electron system, associated with a modulation of the phase of the order parameter.[36,37] The energy of the B. A. mode is proportional to $v_F|\boldsymbol{q}|$, where v_F is the Fermi velocity and $\boldsymbol{q}$ the wave vector. So far we did not consider the Coulomb interaction between the carriers that will shift the mode toward higher frequencies. In a single-layer superconductor (one CuO_2 plane per unit cell), a longitudinal electromagnetic field with $\boldsymbol{E}\parallel c$ would induce a B. A.-like mode with energy proportional to the Fermi velocity along the c-axis v_{Fz}, $v_{Fz}\sim t_\perp$. In the present case of the IR response of a bilayer superconductor the situation is more complicated. The electromagnetic wave is transverse with $\boldsymbol{q}\perp c$. Nevertheless, it induces a charge density that is modulated along the c axis. The modulation is analogous to the one associated with the B. A. mode of a single-layer superconductor with $\boldsymbol{q}\parallel c$, $|\boldsymbol{q}|=\pi/d$ (d is the interplane distance). This is illustrated in Fig. 4. The analogy allows us to interpret the mode as an analog of the B. A. mode. This point of view can be substantiated by comparing the Eqs. (23) and (24) with those describing the longitudinal response of a single-layer superconductor. For $\boldsymbol{E}\parallel c$, $\boldsymbol{q}\parallel c$, $|\boldsymbol{q}|=\pi/d$, and for the Born-Kármán region containing only two planes (a rather artificial situation), the latter possess the same form as the former. Note that the long-wavelength in-plane modulation of the electromagnetic wave has qualitatively no impact on the mode.

Figure 5 shows the $t_\perp$ dependence of the intrabilayer conductivity $\sigma_{bl/bl}$ calculated with (a) the VC neglected and (b) with the VC included. The frequency of the peak in (a) is

http://doc.rero.ch

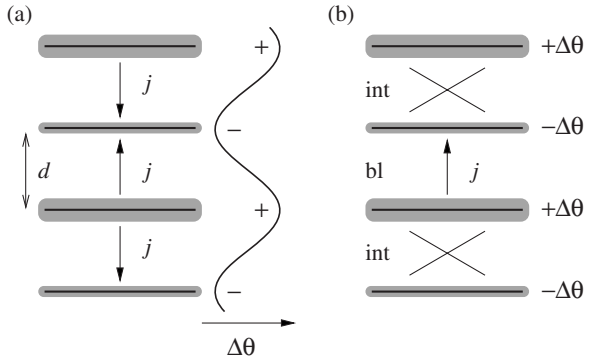

FIG. 4. (a) Schematic representation of the current-density, density, and phase pattern associated with the Bogolyubov-Anderson mode of a single-layer superconductor with $\boldsymbol{q}\|c$, $|\boldsymbol{q}|=\pi/d$. (b) The same for the collective mode of the bilayer system discussed in the text.

determined by $E_{kA}+E_{kB}$, which approaches 2Δ for $t_\perp \to 0$. The energy of the collective mode in (b), however, does not depend on Δ; instead it is proportional to $t_\perp$. This is consistent with the proposed interpretation of the mode and analogous to the relation $\omega(\text{B.A.}) \sim v_F|\boldsymbol{q}|$.

A further insight into the origin of the collective mode can be obtained by using arguments inspired by Anderson's work on gauge invariance and the Meissner effect.[37] Anderson explains the difference between transverse and longitudinal excitations in terms of the complete second-order phonon-mediated interaction between electrons. The impact of the relevant interaction terms on longitudinal and transverse excitations is shown to be fundamentally different. In the longitudinal case, these terms lead to a restoration of the gauge invariance, to the absence of the condensate contribution in the response function, and to the presence of a mode at a finite frequency proportional to the magnitude of the wave vector. In the present case, this role is played by the interaction terms involving the products of the form

$$c^\dagger_{\boldsymbol{k}B\uparrow} c^\dagger_{-\boldsymbol{k}A\downarrow} c_{-\boldsymbol{k}'A\downarrow} c_{\boldsymbol{k}'B\uparrow} \quad \text{and} \quad c^\dagger_{\boldsymbol{k}A\uparrow} c^\dagger_{-\boldsymbol{k}B\downarrow} c_{-\boldsymbol{k}'B\downarrow} c_{\boldsymbol{k}'A\uparrow}. \quad (31)$$

They do not belong to the reduced BCS Hamiltonian leading to Eq. (11). They have, however, a profound impact on the final states since they provide an attractive interaction between "elementary excited states," i.e., the states created by operators $c^\dagger_{\boldsymbol{k}A\uparrow} c_{\boldsymbol{k}B\uparrow}$ and $c^\dagger_{\boldsymbol{k}A\downarrow} c_{\boldsymbol{k}B\downarrow}$, that appear in the expressions for the current-density operators on the right-hand side of Eq. (12). The resulting bound state, i.e., the mode behind the maximum in the spectra, can be thought of as equivalent to a Cooper bound state of a pair of electrons—one from the bonding band and the other from the antibonding band—superimposed on the BCS ground state of the two bands.

It has been shown that the B. A. mode can be associated with oscillations of the phase of the order parameter. We have checked that for small values of $t_\perp$ the collective mode of our bilayer case can be similarly associated with oscillations of the relative phase of the two planes. The pattern of the phase modulation is shown in Fig. 4. Finally, the mechanism of the increase in the frequency of the mode when going from the local conductivity $\sigma_{\text{bl/bl}}$ to the total conductivity, involving the Coulomb interaction of the charged planes, is an analog of the Anderson-Higgs mechanism.

Next we address the more complicated case of $t'_\perp \neq 0$, where the theory involves the four local conductivities defined by Eq. (18): $\sigma_{\text{bl/bl}}$, $\sigma_{\text{bl/int}}$, $\sigma_{\text{int/bl}}$ (that differs from $\sigma_{\text{bl/int}}$ only by a factor of $d_{\text{bl}}/d_{\text{int}}$), and $\sigma_{\text{int/int}}$. Figure 6(a) shows the real parts of $\sigma_{\text{bl/bl}}$, $\sigma_{\text{bl/int}}$, and $\sigma_{\text{int/int}}$ for representative values of the hopping parameters.

The dashed (solid) lines correspond to the NV approximation (to the approach with the VC included). In the NV case, all the conductivities display a pronounced structure around 100 meV: a maximum in Re $\sigma_{\text{bl/bl}}$ and Re $\sigma_{\text{int/int}}$, and a wavelike feature in Re $\sigma_{\text{bl/int}}$. The VC leads to drastic changes in Re $\sigma_{\text{bl/bl}}$. The maximum shifts toward lower energies and its spectral weight (SW) increases on the account of the condensate (not shown). On the other hand, the structures in Re $\sigma_{\text{int/int}}$ and Re $\sigma_{\text{bl/int}}$ remain qualitatively the same and, in particular, they do not shift toward lower energies.

The difference can be understood using Fig. 7. Part (a) provides a schematic representation of the Wannier-type orbitals of the planes and of the interplane hopping processes. For $t'_\perp \ll t_\perp$, it is useful to consider bonding and antibonding orbitals of the individual bilayers shown in (b), $\Psi_B = (1/\sqrt{2})[\Psi_1+\Psi_2]$, $\Psi_A = (1/\sqrt{2})[\Psi_1-\Psi_2]$. The local current densities and conductivities can be discussed and understood in terms of the transitions denoted by the arrows. The intrabilayer current-density operator is connected with transitions within individual bilayers, marked by the solid arrows. Note that these transitions create *two quasiparticles from the same bilayer unit*. The interbilayer current-density operator is connected with transitions between adjacent bilayers, marked by the dashed arrows. These transitions create *two quasiparti-*

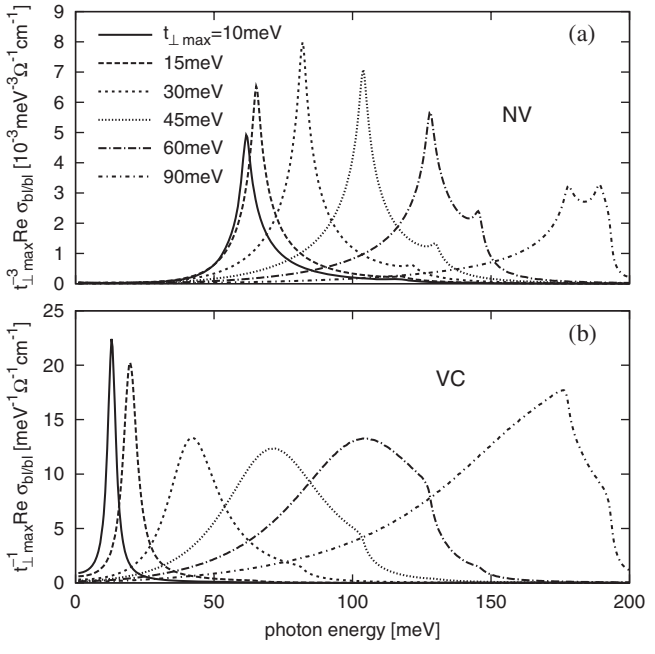

FIG. 5. Dependence of the real part of the local conductivity $\sigma_{\text{bl/bl}}(T=20\ \text{K})$ on the intrabilayer hopping amplitude $t_{\perp\,\max}$ calculated with the vertex corrections neglected (a) and included (b). In (a), the absorption peak stops at $2\Delta_{\max}=60$ meV when decreasing $t_{\perp\,\max}$. In (b), the energy of the peak is proportional to $t_{\perp\,\max}$.

http://doc.rero.ch

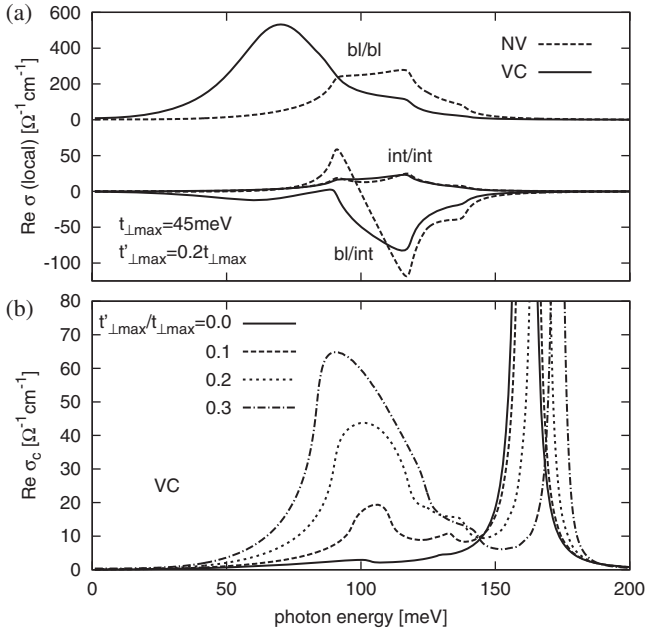

FIG. 6. (a) Real parts of the local conductivities $\sigma_{\mathrm{bl/bl}}$, $\sigma_{\mathrm{bl/int}}$, and $\sigma_{\mathrm{int/int}}$ calculated considering the BCS interaction between the charged quasiparticles for $t_{\perp\,\mathrm{max}}$=45 meV, $t'_{\perp\,\mathrm{max}}$=0.2$t_{\perp\,\mathrm{max}}$, Δ_{max} =30 meV, and T=20 K. The spectra of Re $\sigma_{\mathrm{bl/int}}$ and Re $\sigma_{\mathrm{int/int}}$ are four times magnified. The dashed (solid) lines correspond to the NV approximation (to the approach with the VC included). (b) Real part of the total c-axis conductivity calculated using Eq. (4) for various values of the ratio $t'_{\perp\,\mathrm{max}}/t_{\perp\,\mathrm{max}}$. The figure demonstrates the effect of the interbilayer hopping.

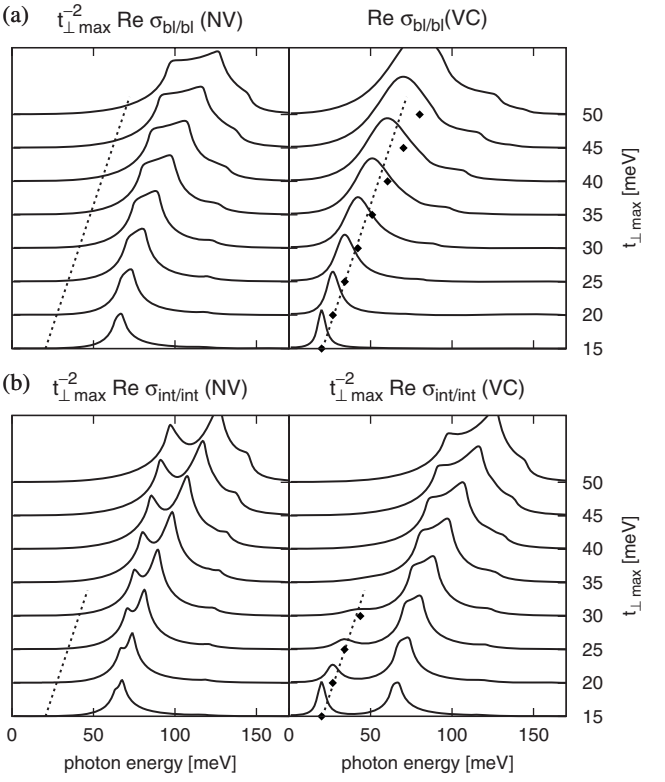

FIG. 8. Dependence of (a) Re $\sigma_{\mathrm{bl/bl}}$ and (b) Re $\sigma_{\mathrm{int/int}}$ on the hopping amplitude $t_{\perp\,\mathrm{max}}$. A constant value of the ratio $t'_{\perp\,\mathrm{max}}/t_{\perp\,\mathrm{max}}$ of 0.2 has been used. If the vertex corrections are included, the B. A.-like mode characterized by a linear $t_\perp$ dependence appears in the bl/bl component and, for small values of $t_{\perp\,\mathrm{max}}$, also in the int/int component.

cles from different units. The important point is that the final states due to the former (latter) transitions are strongly (weakly) modified by the VC because *the interactions are restricted to individual bilayers*. This is the reason why $\sigma_{\mathrm{bl/bl}}$ [determined by the matrix element of Eq. (20) involving states generated by $\hat{j}^p_{\mathrm{bl}}$, i.e., by the former transitions] is strongly influenced by the VC, whereas $\sigma_{\mathrm{int/int}}$ [determined by the matrix element of Eq. (20) involving states generated by $\hat{j}^p_{\mathrm{int}}$, i.e., by the latter transitions] hardly changes. The changes in $\sigma_{\mathrm{bl/int}}$ are more complex because different final states are involved: one due to the former transitions and the other due to the latter transitions.

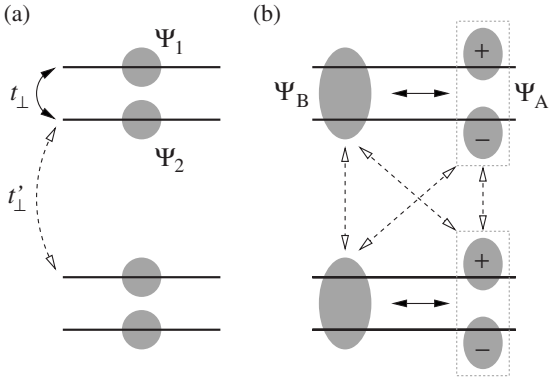

FIG. 7. Scheme illustrating the differences between the local conductivities $\sigma_{\mathrm{bl/bl}}$ and $\sigma_{\mathrm{int/int}}$. The Wannier-type orbitals of the planes are denoted by Ψ_1 and Ψ_2, the bonding and antibonding orbitals of the individual bilayers by Ψ_A and Ψ_B, respectively. The current-density operators $\hat{j}^p_{\mathrm{bl}}$ and $\hat{j}^p_{\mathrm{int}}$ can be associated with transitions marked by the solid and the dashed arrows, respectively.

The $t_\perp$ dependencies of Re $\sigma_{\mathrm{bl/bl}}$ and Re $\sigma_{\mathrm{int/int}}$ are contrasted in Fig. 8. It can be seen that the VC cause qualitative changes in Re $\sigma_{\mathrm{bl/bl}}$, in particular, they lead to the linear $t_\perp$ dependence of the frequency of the maximum. The spectra of Re $\sigma_{\mathrm{int/int}}$, on the other hand, do not change qualitatively, except for the very small values of $t_\perp$, where the B. A.-like mode appears even in the interlayer conductivity.

The structures of the conductivities $\sigma_{\mathrm{int/int}}$ and $\sigma_{\mathrm{bl/int}}$ give rise—via the multilayer formula—to a maximum in the spectra of Re σ_c as shown in part (b) of Fig. 6. It can be seen that the magnitude of the peak is proportional to $t'^2_\perp$. The maximum of Re $\sigma_{\mathrm{int/int}}$ and the related peak of Re σ_c can be interpreted simply as an interband bonding-antibonding pair-breaking (coherence) peak, with the coherence factor proportional to the magnitude of the band splitting. We recall that in one-band superconductors, the conductivity does not exhibit any coherence peak around 2Δ due to the fact that electromagnetic absorption belongs to phenomena governed by case II coherence factors.[31,38] Here the situation is different because of the presence of the two bands.

http://doc.rero.ch

http://doc.rero.ch

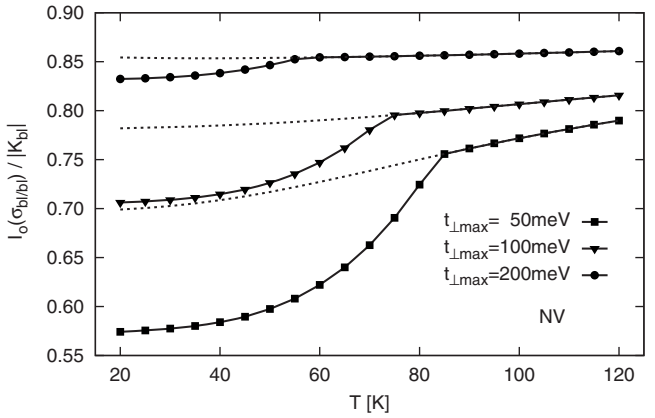

FIG. 9. Optical weight $I_o = 2\hbar^2/\pi e^2 \int_{0^+}^{\infty} \mathrm{Re}\ \sigma_{bl}(\omega) \mathrm{d}\omega$ of the local conductivity σ_{bl} divided by $|K_{bl}|$ as a function of temperature for various values of the interplane hopping parameter $t_\perp$. Here K_{bl} is the effective c-axis kinetic energy defined by Eq. (19). The results were obtained using Eq. (21) within the spin-fermion model with no interbilayer hopping ($t'_{\perp\ max}=0$) and the resonant mode in the odd-interaction channel only, the vertex corrections have been neglected. With the inclusion of the vertex corrections, $I_o/|K_{bl}|$ is always equal to 1, both for the normal and the superconducting states.

B. Quasiparticles coupled to spin fluctuations

Here we discuss the c-axis response obtained by the self-consistent computations within the spin-fermion model. As in Sec. III A, we begin with the simpler case of $t'_\perp = 0$. Interestingly, the VC plays an important role even in the normal state, an effect that was not addressed at the BCS level. In particular, for the NS local conductivity calculated with the VC neglected, the restricted conductivity sum rule

$$I_o = \frac{2\hbar^2}{\pi e^2} \int_{0^+}^{\infty} \mathrm{Re}\ \sigma_{bl}(\omega) \mathrm{d}\omega = -K_{bl} \tag{32}$$

is strongly (by tens of percent) violated. This is demonstrated in Fig. 9. It can be seen that the deficiency is more serious for smaller values of the band splitting. With the VC included, the sum rule is satisfied. Let us note that the corresponding violation of the in-plane sum rule is an order of magnitude weaker.[22]

Changes in $\sigma_{bl/bl}$ caused by the incorporation of the VC are so pronounced that there is not much similarity between the NV and the VC spectra (see Fig. 10). The NS spectra for the NV case shown in (a) display a broad low-energy absorption band corresponding to bonding-antibonding interband transitions, which can be compared with the sharp absorption structure of the NS spectra of the BCS case. The broadening with respect to the BCS case is due first to the finite lifetime of the quasiparticles and second to the presence of a pronounced incoherent background of the spectral function. The VC shift the absorption band toward higher energies [see part (b)]. This can be understood in terms of the complete second-order spin-fluctuation-mediated interaction between the electrons: the relevant terms can be shown to correspond to a repulsive coupling of the excited states with one electron in the antibonding band and one hole in the bonding band. In

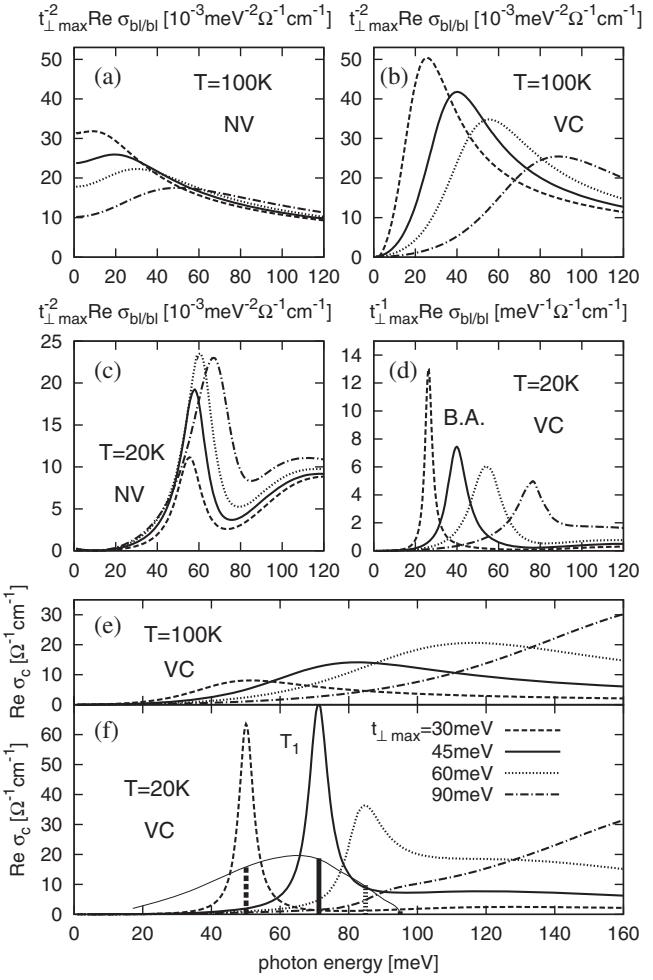

FIG. 10. Effect of the vertex corrections on the conductivities. Real parts of [(a)–(d)] the local conductivity $\sigma_{bl/bl}$ and of [(e)-(f)] the total c-axis conductivity calculated within the spin-fermion model. The spacing layers have been taken to be insulating, i.e., $t'_{\perp\ max}=0$ and the neutron resonance has been included in the odd-interaction channel only. Results for several values of the hopping parameter $t_{\perp\ max}$ are presented. The spectra in (a) and (c) [(b), (d), (e), and (f)] have been obtained for the NV (VC) case. The thin line in (f) represents the estimated energy dependence of the spectral weight of the peak labeled as T_1. For $t_{\perp\ max}=30$ meV (45 meV, 60 meV), the estimated value of the spectral weight is 4000 Ω^{-1} cm^{-2} (4600 Ω^{-1} cm^{-2}, 2300 Ω^{-1} cm^{-2}).

the total c-axis conductivity shown in Fig. 10(e) the band is shifted even further and it is very broad.

The spectra of the SC state for the NV case as shown in Fig. 10(c) display a pair-breaking peak at about 2Δ, corresponding to a similar feature of the BCS case, and a continuum with an onset around 80 meV. In addition, Re $\sigma_{bl/bl}$ also contains the contribution of the condensate $\sim\delta(\omega)$ (not shown). The VC transforms the spectra in a similar way as in the nonretarded case [see part (d)]. They destroy the condensate and the pair-breaking peak; instead, a sharp maximum (mode) appears, whose energy is proportional to $t_\perp$. As discussed in Sec. III A, the mode can be interpreted as an analog of the B. A. mode. In the following we shall call it simply B. A. mode. In the total c-axis conductivity, see Fig.

http://doc.rero.ch

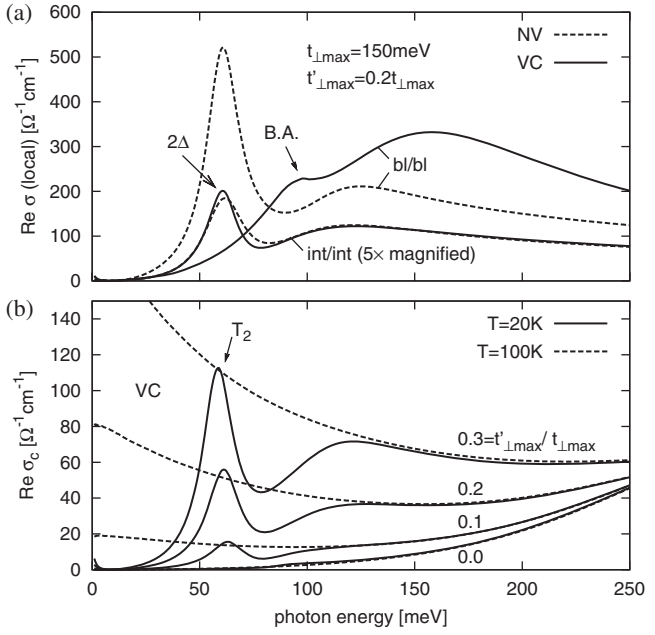

FIG. 11. Effect of finite interbilayer hopping ($t'_{\perp\,\mathrm{max}}>0$) on the conductivities. Real parts of (a) the local conductivities $\sigma_{\mathrm{bl/bl}}$ and $\sigma_{\mathrm{int/int}}$ and of (b) the total c-axis conductivity calculated within the spin-fermion model. The neutron resonance has been distributed equally in both (even and odd) interaction channels. The dashed (solid) lines in (a) represent the spectra obtained with the VC neglected (included). The spectra in (b) have been obtained with the VC included, the dashed (solid) lines correspond to the normal (superconducting) state, results for several values of $t'_{\perp\,\mathrm{max}}$ are shown.

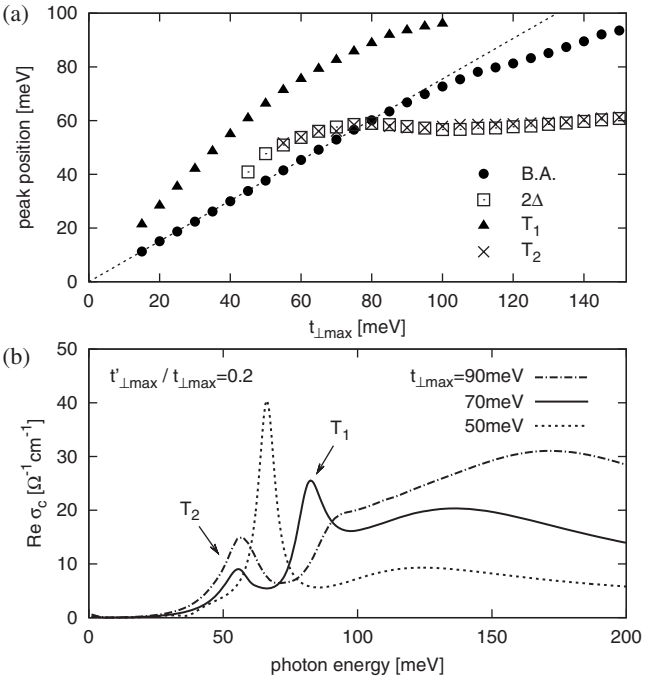

FIG. 12. (a) Energies of the B. A. peak and of the 2Δ peak in the local conductivity $\sigma_{\mathrm{bl/bl}}$, and of the structures T_1 and T_2 in the total c-axis conductivity (for examples, see Figs. 10 and 11) as a function of the intrabilayer hopping parameter $t_{\perp\,\mathrm{max}}$. A constant value of the ratio $t'_{\perp\,\mathrm{max}}/t_{\perp\,\mathrm{max}}$ of 0.2 has been used. (b) Real part of the total conductivity for values of $t_{\perp\,\mathrm{max}}$, where both structures T_1 and T_2 are visible. As $t_{\perp\,\mathrm{max}}$ decreases, the peak T_1 emerges from the background at $t_{\perp\,\mathrm{max}}\approx 100$ meV, and it quickly becomes the dominant feature. Eventually, it covers the T_2 peak at $t_{\perp\,\mathrm{max}}\approx 50$ meV.

10(f), the mode is shifted toward higher energies by virtue of the Coulomb effects associated with the charging of the planes, the corresponding peak will be labeled as T_1. Let us emphasize that the sharp peak shows up only in the superconducting state, the presence of a narrow mode in χ_{SF} is not a sufficient condition for its appearance.

In the remaining part of this subsection, we address the case of nonzero $t'_\perp$. Similarly as in the BCS case, the impact of the VC on $\sigma_{\mathrm{bl/bl}}$ is much stronger than that on the other local conductivities. This is illustrated in part (a) of Fig. 11. The NV spectra of Re $\sigma_{\mathrm{bl/bl}}$ exhibit a pair-breaking peak at about 2Δ, similar as in Fig. 10(c). The VC destroys the peak and leads to the formation of the B. A. mode. For the present value of $t_\perp$ of 150 meV, the mode is located in the region of the continuum [cf. Fig. 10(d)] and, thus, only gives rise to a weak structure around 100 meV. The interbilayer conductivity $\sigma_{\mathrm{int/int}}$, on the other hand, is almost unaffected by the VC, retaining the characteristic maximum at about 2Δ (labeled as 2Δ maximum in the following). The $t_\perp$ dependencies of the energies of the B. A. mode and of the 2Δ peak in the local conductivity are shown in Fig. 12(a). The energy of the B. A. mode can be seen to be proportional to $t_\perp$, except for the region of high values of $t_\perp$; that of the 2Δ peak is approximately $t_\perp$ independent.

The 2Δ maximum appears also in the total c-axis conductivity, as shown in Fig. 11(b). The spectral weight of the corresponding peak (labeled as T_2 in the following) is proportional to $t'^2_\perp$. As documented in Fig. 12(b), for low values of $t_\perp$, T_1 dominates and T_2 cannot be resolved. For high values of $t_\perp$, on the other hand, T_2 is the most pronounced feature since the B. A. mode merges with the continuum and T_1 can hardly be resolved. Both features can be seen for intermediate values of $t_\perp$, e.g., $t_\perp=70$ meV. The $t_\perp$ dependencies of the energies of the structures T_1 and T_2 in the total c-axis conductivity are given in Fig. 12(a).

C. Comparison with experiment and with the theory proposed by Shah and Millis

The c-axis conductivity displays two superconductivity-induced structures (modes): P_1 and P_2 in the experimental data, and T_1 and T_2 in the theoretical spectra. In what follows, we argue that the features P_1 and P_2 can be attributed to T_1 and T_2, respectively.

First, we summarize the relevant trends of the structures P_1 and P_2 as observed in the experimental data of bilayer compounds, in particular Y-123 and related systems. Some of the trends are demonstrated in Fig. 13.

(E1) The frequency of P_1 increases with increasing hole concentration p.[1,2,5,11,12,20,21,40,41]

(E2) The SW of P_1 first increases with increasing p, then saturates for $p\approx 0.12$, and for higher values of p, P_1 broadens and its SW gradually decreases; for $p>0.15$, P_1 cannot be resolved anymore.[20]

http://doc.rero.ch

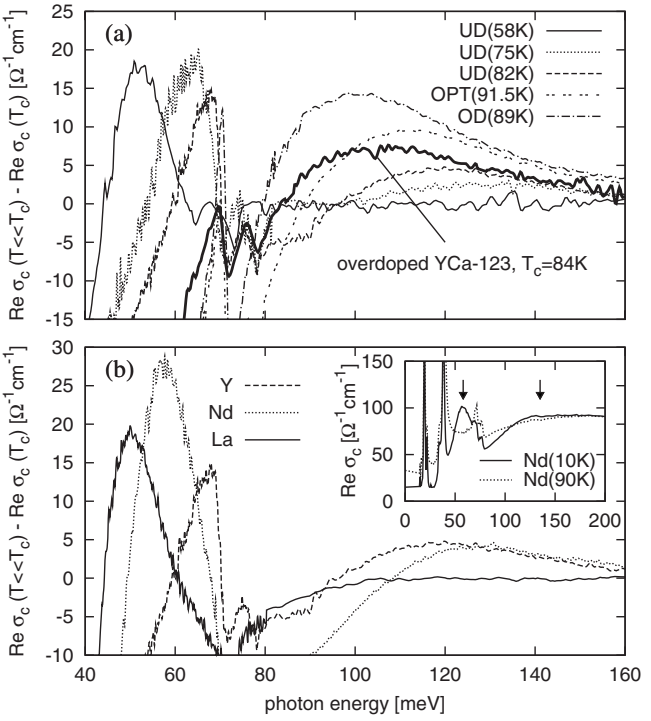

FIG. 13. (a) Doping dependence of the difference Re $\sigma_c(T \ll T_c) - \mathrm{Re}\ \sigma_c(T \approx T_c)$ for Y-123. The abbreviations UD, OPT, and OD stand for underdoped, optimum doped, and overdoped. The values of p are 0.093, 0.116, 0.124, 0.155, and 0.194. Also shown are the data for $Y_{0.86}Ca_{0.14}$-123 with $T_c = 84$ K and $p = 0.176$. Details concerning the samples and the experiment are given in Refs. 20 and 39. (b) The spectra of the difference for the sequence R-123 ($R = Y$, Nd, and La) with $p \approx 0.12$. In this sequence, the distance between the CuO_2 planes within a bilayer increases. The inset shows the original spectra for Nd-123. Adapted from Fig. 2 of Ref. 20.

(E3) The frequency of P_1 decreases when going—for a fixed doping level—from Y-123 over Nd-123 to La-123.[20] In this sequence of materials, the distance between the closely spaced planes increases.

(E4) In the YPr-123 system, the doping level can be modified either by changing the oxygen concentration or by partially replacing Y with Pr. The replacement leads to a decrease in p. By combining the two approaches, it is possible to obtain various combinations of p and the NS dc conductivity along the c axis, σ_{dc}. For a fixed doping, there is no pronounced correlation between the SW of P_1 and σ_{dc}.[21,42]

(E5) The structure P_2 can be resolved only for $p \geq 0.10$.[20]

(E6) The frequency of P_2 slowly decreases with increasing p.[20]

(E7) The SW of P_2 increases with increasing p.[20]

(E8) In the YCa-123 system, it is possible, similarly as in the case of YPr-123, to obtain various combinations of p and σ_{dc}. For a fixed doping, the SW of P_2 increases with increasing σ_{dc}, see Fig. 13.

The distance between the closely spaced planes can be expected to be correlated with the strength of the intrabilayer electronic coupling. The observation (E3), thus, suggests a relation between P_1 and the coupling. Further, the dc conductivity is likely to reflect the strength of the coupling through the spacing layer. The observations (E4) and (E8), thus, seem to imply an independence of P_1 and a dependence of P_2 on this coupling.

Second, we review the corresponding properties of T_1 and T_2 resulting from our computations. The labels (T1)–(T8) are parallel those used in the summary of experimental facts.

(T1) The energy of T_1 increases with increasing $t_\perp$ (see Figs. 5 and 10).

(T2) The SW of T_1 first increases with increasing $t_\perp$, then saturates for $t_\perp \approx 50$ meV, and for higher values of $t_\perp$, T_1 broadens and gradually vanishes [see Fig. 10(f)]. The broadening is due to the fact that T_1 reaches the continuum.

(T4) For a given $t_\perp$, T_1 does not change significantly with increasing $t'_\perp$ (not shown). Note that $t'_\perp$ determines σ_{dc}: σ_{dc} is approximately proportional to $t'^2_\perp$.

(T6) The energy of T_2 is approximately equal to 2Δ for low values of $t_\perp$ and somewhat larger than 2Δ for higher values of $t_\perp$ of the order of 100 meV [see Fig. 12(a)].

(T7) The SW of T_2 increases with increasing $t_\perp$ (not shown).

(T8) The SW of T_2 also increases with increasing $t'_\perp$ (see Fig. 11). For a given $t_\perp$, the SW of T_2 is approximately proportional to $t'^2_\perp$, similarly as σ_{dc}.

A comparison between the items (E1)–(E4) and (T1)–(T4) suggests that P_1 could be attributed to T_1 *provided that* $t_\perp$ increases with increasing p. This crucial assumption is consistent with results obtained using the bilayer t–J model and the Gutzwiller approximation.[43,44] Alternatively, it can also be justified considering a PG competing with superconductivity and the reported p and $\boldsymbol{k}$ dependencies of the magnitude of the PG and of the coherence peaks due to superconductivity.[45,46] With decreasing p, the magnitude of the PG increases and the area of the part of the Brillouin zone dominated by the PG, centered around the antinode, expands. At the same time, the area of the part with pronounced Bogolyubov quasiparticles shrinks toward the BZ diagonal. The important point is that at the BZ diagonal, $t_\perp$ is probably the smallest.[9] The shrinkage of the area of strong superconducting correlations might, thus, lead to a decrease in an effective $t_\perp$ determining the energy of the low-energy mode.

The properties (E5)–(E8) are in agreement with attributing P_2 to T_2: The items (E5) and (E7) can be understood in terms of (T7) and (T8), when combined with the assumption of $t_\perp \sim p$ and with the obvious fact that $t'_\perp$ increases with increasing oxygen concentration; (E6) is consistent with (T6), when combined with the experimental fact that around optimum doping, Δ decreases with increasing p. Further, (E8) can be understood based on (T8).

An obvious problem of the proposed assignment of T_1 to P_1 and T_2 to P_2 is that $\omega(T_1) > \omega(T_2)$ for the relevant range of parameters (see Fig. 12), whereas for underdoped materials with $0.10 < p < 0.15$ the frequency of P_1 is lower than that of P_2.[20] The reason for this discrepancy is probably the following: Experimentally, $\omega(P_2) \approx 100$ meV which requires $\Delta \approx 50$ meV, and such a high value cannot be achieved using the present self-consistent theory with reasonable values of input parameters. The effective gap may have a contribution due to the pseudogap, which is not included in the

http://doc.rero.ch

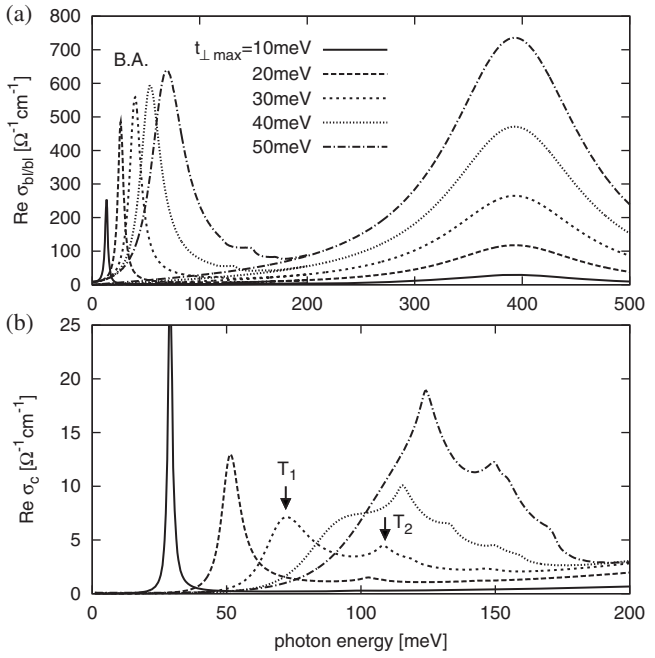

FIG. 14. Illustrates the potential of the model to provide the order of the spectral structures consistent with experimental data on underdoped Y-123. (a) Real part of the local conductivity $\sigma_{bl/bl}$ consisting of the result of the BCS approach with Δ=50 meV and a broad Lorentzian described in the text. (b) Real part of the total c-axis conductivity obtained using the local conductivity $\sigma_{bl/bl}$ shown in (a) and the other three local conductivities resulting from the BCS approach. A constant value of the ratio $t'_{\perp\,max}/t_{\perp\,max}$ of 0.2 has been used.

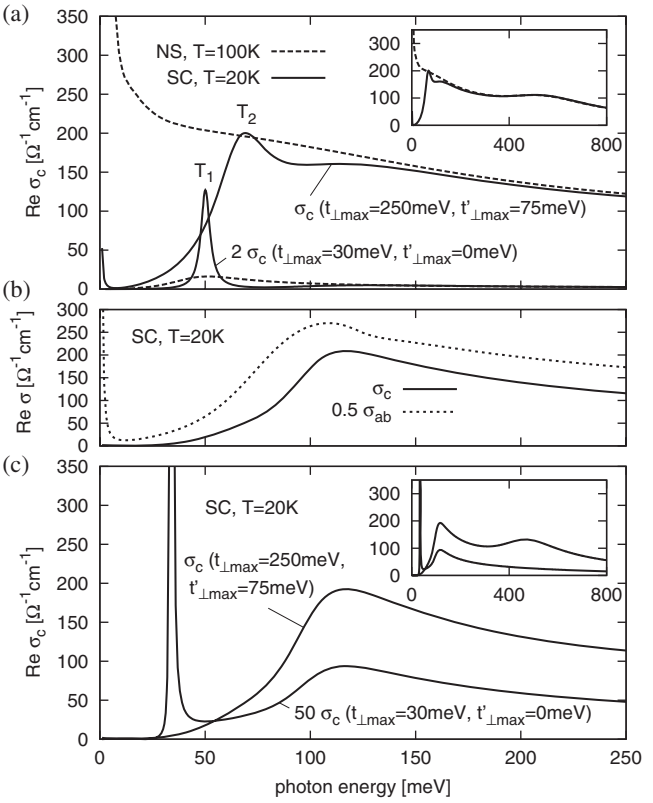

FIG. 15. Representative examples of the spectra of Re σ_c compared with the conductivities of a related single-layer system, and with the spectra of the same quantity obtained using the approximation proposed by Shah and Millis. (a) Real part of the total c-axis conductivity calculated using the spin-fermion model with $t_{\perp\,max}$ =250 meV, $t'_{\perp\,max}$=75 meV, and with $t_{\perp\,max}$=30 meV, $t'_{\perp\,max}$ =0 meV. The solid and the dashed lines correspond to the superconducting and the normal state, respectively. The spectra for $t_{\perp\,max}$=250 meV and $t'_{\perp\,max}$=75 meV on an extended scale are shown in the inset. (b) Real parts of the in-plane conductivity and of the c-axis conductivity for a single-layer superconductor with the plane spacing of $d_{bl}+d_{int}$ and with the c-axis hopping parameter of the form of Eq. (7) and the maximum of 75 meV. (c) The same as in (a) but using the approach proposed by Shah and Millis, where the nondiagonal components of the conductivity $\sigma_{bl/int}$ and $\sigma_{int/bl}$ are neglected, and the diagonal component $\sigma_{bl/bl}$ ($\sigma_{int/int}$) is approximated by the conductivity of the single-layer superconductor with the hopping parameter equal to $t_\perp$ ($t'_\perp$). Only the superconducting state spectra are shown.

present theory. Within the BCS approach, Δ is an input parameter. Unfortunately, the resulting spectra of σ_c for the interesting region of the parameter space ($\Delta > t_\perp$) contain overlapping resonances that cannot be easily disentangled. The complication is due to the absence of an incoherent background in the local conductivities. Motivated by this observation, we have supplemented the component $\sigma_{bl/bl}$ with a broad Lorentzian, $-iA/(\omega_L^2-\omega^2-i\omega\Gamma_L)$, ω_L=0.4 eV, Γ_L =0.15 eV, and $A\sim t_\perp^2$. The $t_\perp$ dependence of the spectral-weight parameter A is consistent with Eq. (21). The results are shown in Fig. 14. It can be seen that the $t_\perp$ dependence of the total conductivity shown in (b) resembles the doping dependence of the data,[20] including the interplay of T_1 and T_2: For low values of $t_\perp$, the spectra are dominated by T_1; for intermediate values of 20–30 meV, both spectral structures are present, and with increasing $t_\perp$, T_1 gradually hides in the continuum.

The discrepancy in the order of the spectral structures does not occur for optimally doped and overdoped Y-123 samples, where P_1 is buried in the continuum part of the spectra located above the maximum P_2. The experimental spectra (see, e.g., Fig. 1 of Ref. 12) are similar to the calculated ones corresponding to the values of $t_\perp$ of a few hundreds of meV. As an example, we show in Fig. 15(a) the NS and SC-state spectra of Re σ_c corresponding to $t_{\perp\,max}$ =250 meV and $t'_{\perp\,max}$=0.3$t_{\perp\,max}$. The maximum T_2 at about 70 meV (600 cm^{-1}) probably corresponds to P_2 occurring at a slightly higher frequency in the experimental spectra.

Next we compare our calculated spectra of Re σ_c with the conductivities of a related single-layer superconductor and with those computed along the lines of the theory proposed by Shah and Millis (SM).[14] Figure 15(a) shows, besides the spectra of Re $\sigma_c(t_{\perp\,max}$=250 meV,$t_{\perp\,max}$=75 meV) discussed above, those corresponding to $t_{\perp\,max}$=30 meV and $t_{\perp\,max}$=0 meV. The former (the latter) represent the case of strong (weak) intrabilayer coupling. The corresponding renormalized values of the (normal-state) bilayer splitting are ca 80 and 10 meV. Note that the former value is close to that of Bi-2212 as obtained by photoemission experiments.[16–19] As discussed in the context of Figs. 11 and 12 only one peak is present in the superconducting state spectra: T_2 in the

http://doc.rero.ch

former case and T_1 in the latter. It is instructive to compare the SC-state conductivities with the solid line of Fig. 15(b) representing the c-axis conductivity of a model single-layer superconductor described in the caption. This allows one to identify the features specific to the bilayer compounds: (i) the peak T_1 (for small values of $t_\perp$), (ii) the peak T_2 (for large values of $t_\perp$ and $t'_\perp \neq 0$), and (iii) a hump in the midinfrared (for large values of $t_\perp$). For $t_{\perp\,\mathrm{max}}=250$ meV, the hump is centered at 500 meV. It has the same origin as the 160 meV maximum in Fig. 3 and it can be attributed to the (upper) plasma mode of the bilayer unit [see the discussion following Eq. (30)]. Both T_1 and T_2 would appear for intermediate values of $t_\perp$, as discussed in the context of Figs. 12 and 14. The broad band centered around 120 meV in Fig. 15(a) appears also in the conductivity of the single-layer superconductor and is, thus, not specific to the bilayer compounds.

Also shown in Fig. 15(b) is the in-plane conductivity of the single-layer superconductor. It can be seen that the shapes of the two conductivities are fairly similar. The main differences are: (a) for $T=20$ K, a narrow Drude term can be resolved only in Re σ_{ab}, and (b) the onset of Re σ_c is more gradual than that of Re σ_{ab}. Both (a) and (b) are due to the difference between the matrix element of σ_{ab}, i.e., the in-plane quasiparticle velocity, and $t_\perp$. Both σ_{ab} and σ_c exhibit a maximum around 110 meV and both decrease with increasing energy above this maximum. The origin of the maximum has been addressed in Refs. 22 and 32. The calculated c-axis conductivity of the single-layer superconductor is qualitatively similar to the measured conductivity of $La_{2-x}Sr_xCuO_4$ reported in Ref. 47.

Figure 15(c) shows the c-axis conductivities of the same bilayer systems as in (a), but calculated using the approach proposed by SM, where the nondiagonal components of the conductivity $\sigma_{\mathrm{bl/int}}$ and $\sigma_{\mathrm{int/bl}}$ are neglected, and the diagonal component $\sigma_{\mathrm{bl/bl}}(\sigma_{\mathrm{int/int}})$ is approximated by the conductivity of the single-layer superconductor with the hopping parameter equal to $t_\perp(t'_\perp)$. When calculating the latter conductivities, SM further replace the k_z-dependent Green's function with a k_z-independent one of a two-dimensional model. Instead of using this approximation, we have obtained the conductivities of the model single-layer superconductors by scaling the one shown in Fig. 15(b). We have checked that for the present values of the parameters, the results of the two approaches are almost the same. By comparing panels (a) and (c) of Fig. 15, we easily identify differences between the SM theory that does not involve the bilayer splitting and our improved approach that does. For small values of $t_\perp$, the SM theory provides a peak inside the gap, corresponding to a bilayer plasmon, similar to the transverse Josephson plasmon of the phenomenological model.[13] The T_1 peak of our theory is located at a slightly higher energy and its interpretation is different. What it has in common with the transverse Josephson plasmon is that both are associated with oscillations of the relative phase of the two closely spaced planes. For high values of $t_\perp$, our approach yields the pair-breaking peak T_2 absent at the SM level. At high energies (above 100 meV), the results of the two approaches are similar.

Interestingly, the NS spectra corresponding to $t_{\perp\,\mathrm{max}}=250$ meV shown in Fig. 15(a) do not display any clear signature of the bilayer splitting, consistent with experimental data. The contribution of the bonding-antibonding transitions is hidden in the midinfrared region. This is because the renormalization of the quasiparticles leads to a very broad absorption band [see Fig. 10(a)] shifted toward the midinfrared both by the vertex corrections and by the Coulomb effects [see Figs. 10(b) and 10(e)].

Experiments reveal an increase in the optical spectral weight in the far-infrared below T_c, with a possible interpretation in terms of a decrease in the c-axis kinetic energy associated with the superconducting transition.[48] The picture resulting from our calculations, restricted to the case of small values of $t_{\perp\,\mathrm{max}}$ and $t'_{\perp\,\mathrm{max}}=0$, is the following: Below T_c, the peak T_1 forms, gaining spectral weight from a broad interval of energies, and the spectral weight at low energies increases. The total spectral weight, proportional to the negatively taken effective kinetic energy K_{bl}, decreases, provided that χ_{SF} (below T_c) $=\chi_{\mathrm{SF}}$ (above T_c). However, changes in χ_{SF} upon entering the superconducting state, in particular the formation of the resonance mode, can lead to a slight increase in the total spectral weight and the corresponding decrease in K_{bl}, the mechanism being connected to that outlined in Ref. 49. The issue is fairly complex and will be addressed in a separate publication.

IV. SUMMARY AND CONCLUSIONS

We have constructed a realistic microscopic model of the c-axis infrared response of bilayer cuprate superconductors, allowing us to interpret the superconductivity-induced modes occurring in the experimental data.

For the simpler case of insulating spacing layers, the local conductivity of the intrabilayer region does not possess a condensate contribution in the superconducting state [$\delta(\omega)$ in Re σ] as assumed within the phenomenological Josephson superlattice model. Instead, it displays a collective mode at a finite frequency that is proportional to the interplane hopping amplitude $t_\perp$. This has been shown to be a consequence of the gauge invariance. The nature of the mode is similar to that of the Bogolyubov-Anderson mode that participates in the longitudinal response of a homogeneous superconductor. It is associated with charge oscillations between the planes and, for small values of $t_\perp$, also with oscillations of the relative phase of the two planes. This physical picture is fairly similar to that of the transverse plasmon of the Josephson superlattice model. In the total c-axis conductivity the mode is shifted toward higher energies by the interplane Coulomb interaction.

A nonzero amplitude of the hopping through the spacing layer implies a finite conductivity of this layer. This local conductivity exhibits a peak at a frequency slightly higher than $2\Delta_{\mathrm{max}}$, which can be interpreted as a pair-breaking peak. The simple picture is such that two Bogolyubov quasiparticles are involved: one from the bonding band and the other from the antibonding. The reason why the peak appears in the interbilayer conductivity and not in the intrabilayer one is the following. Excited states behind the former (latter) conductivity involve quasiparticles from different bilayers (from the same bilayer). Only the latter are, thus, strongly modified by including the final-state interactions, which are restricted

to individual bilayers. The peak permeates into the total c-axis conductivity.

A series of arguments has been presented assigning the collective mode to the low-energy superconductivity-induced mode of the experimental data (interpreted previously in terms of the Josephson superlattice model) and the pair-breaking maximum to the superconductivity-induced peak centered around 1000 cm^{-1}. The arguments concern the doping dependence of the frequencies and the spectral weights of the peaks and the impact of various substitutions. A crucial assumption, connecting the theory and the experiment, is that the effective $t_\perp$ decreases with decreasing doping. The trends of the underdoped regime, in particular, the appearance of the collective mode below T_c, the increase in its frequency with increasing doping, and its disappearance below optimum doping can all be reasonably reproduced and understood using this assumption. Admittedly, the values of $t_\perp$ of a few tens of meV needed to fit the data are smaller than those deduced from photoemission experiments. The main features of the data of optimally doped Y-123 can be reasonably reproduced with $t_{\perp\,\max}$ of 250 meV, which corresponds to the maximum distance between the renormalized bands of ca 80 meV.

ACKNOWLEDGMENTS

This work was supported by the Ministry of Education of Czech Republic (Grant No. MSM0021622410) and the Schweizerische Nationalfonds (SNF) (Grant No. 200020-119784). In an early stage of this research, during a stay at MPI Stuttgart, D.M. was supported by the AvH Foundation. J.C. thanks B. Keimer and G. Khaliullin for their hospitality during a stay at MPI Stuttgart, where a part of this work was performed. We gratefully acknowledge helpful discussions with Li Yu, A. Dubroka, J. Humlíček, B. Keimer, R. Zeyher, and J. Vašátko.

APPENDIX: BCS LEVEL OF THE THEORY

In this appendix, we show several results obtained at the BCS level, where extensive analytical simplifications can be made. For the sake of brevity, we restrict ourselves to the case of $t'_{\perp k_\parallel}=0$. We employ the BCS interaction of d-wave symmetry which acts in the individual CuO_2 planes (labeled as 1 and 2) within a bilayer unit. The corresponding Hamiltonian reads

$$\hat{H}_{\rm BCS}=\sum_{k\sigma}\varepsilon_{Bk}c^\dagger_{Bk\sigma}c_{Bk\sigma}+\sum_{k\sigma}\varepsilon_{Ak}c^\dagger_{Ak\sigma}c_{Ak\sigma}+\sum_{kk',n\in\{1,2\}}2V_{kk'}c^\dagger_{nk\uparrow}c^\dagger_{n,-k\downarrow}c_{n,-k'\downarrow}c_{nk'\uparrow},\quad\text{(A1)}$$

where $V_{kk'}$ is introduced in the main text. The factor of 2 is for later convenience. The interaction term can be written as

$$\sum_{kk'}V_{kk'}(BBBB+BBAA+AABB+AAAA+BABA+BAAB+ABAB+ABBA),\quad\text{(A2)}$$

where $BBBB$, e.g., stands for $c^\dagger_{Bk\uparrow}c^\dagger_{B,-k\downarrow}c_{B,-k'\downarrow}c_{Bk'\uparrow}$. The first four terms in Eq. (A2) provide the pairing interactions, the other four terms play an important role in the vertex corrections. The above pairing interaction is equally distributed among the two symmetry channels and produces the same gap in both bands, hence, $\Sigma_{A/B}(k)=-\Delta_k\tau_1$ with Δ_k determined by Eq. (11).

Because the self-energy depends on k only, we can sum over the Matsubara frequencies explicitly. The evaluation of the NV response function given by Eq. (21) leads to

$$\begin{aligned}\Pi^{\rm NV(1)}_{\rm bl-bl}(q=0,\hbar\omega)&=-\frac{e^2}{\hbar^2}\frac{d_{\rm bl}}{Na^2}\sum_k t^2_{\perp k}\\&\times\Big\{l_1[1-n_F(E_{Ak})-n_F(E_{Bk})]\\&\times\left(\frac{1}{\hbar\omega+E^+_k+i\delta}-\frac{1}{\hbar\omega-E^+_k+i\delta}\right)\\&+l_2[n_F(E_{Ak})-n_F(E_{Bk})]\\&\times\left(\frac{1}{\hbar\omega+E^-_k+i\delta}-\frac{1}{\hbar\omega-E^-_k+i\delta}\right)\Big\},\end{aligned}\quad\text{(A3)}$$

where $E^\pm_k=E_{Ak}\pm E_{Bk}$ and $l_{1/2}$ are the coherence factors

$$l_{1/2}=\frac{\varepsilon_{Ak}\varepsilon_{Bk}+\Delta_{Ak}\Delta_{Bk}}{E_{Ak}E_{Bk}}\mp 1.\quad\text{(A4)}$$

Note that in the limit of $t_{\perp k}\to 0$, the factors l_1 as well as $n_F(E_{Ak})-n_F(E_{Bk})$ vanish and $\Pi_{\rm bl-bl}$ becomes zero. For the same reason, there is no intraband contribution [Eq. (22)] in the BCS case.

The renormalized vertices Γ_{AB} and Γ_{BA} satisfy the Bethe-Salpeter equations similar to Eq. (24), now containing the BCS interaction

$$\begin{aligned}\Gamma_{AB}(k,iE,i\hbar\nu)=t_{\perp k}\tau_0-\frac{k_BT}{N}\sum_{k',iE'}V_{kk'}&\times\tau_3[\mathcal{G}_B(k',iE')\Gamma_{AB}(k',iE',i\hbar\nu)\\&\times\mathcal{G}_A(k',iE'+i\hbar\nu)\\&+\mathcal{G}_A(k',iE')\Gamma_{BA}(k',iE',i\hbar\nu)\\&\times\mathcal{G}_B(k',iE'+i\hbar\nu)]\tau_3.\end{aligned}\quad\text{(A5)}$$

Since the usual BCS interaction couples with τ_3, not with τ_0 like the spin fluctuations, the above equation contains the additional matrices τ_3. The corresponding equation for the vertex Γ_{BA} differs from Eq. (A5) in the sign of the $t_{\perp k}\tau_0$ term only. By inserting the form of $V_{kk'}$ explicitly, one finds that the vertices can be cast to: $\Gamma_{AB}(k,i\hbar\nu)=t_{\perp k}\tau_0+\lambda w_k C(i\hbar\nu)$ and $\Gamma_{BA}(k,i\hbar\nu)=-t_{\perp k}\tau_0+\lambda w_k C(i\hbar\nu)$. The quantity $C(i\hbar\nu)$ is a 2×2 matrix, independent of iE because of the nonretarded BCS interaction and independent of k because of the separable form of $V_{\mathbf{k}\mathbf{k}'}$. We express it as a linear combination of the Pauli matrices: $C(i\hbar\nu)=\Sigma^3_{\alpha=0}\tau_\alpha C_\alpha(i\hbar\nu)$. The Bethe-Salpeter Eq. (A5) can be then converted to a linear system of equations for the coefficients $C_\alpha(i\hbar\nu)$,

http://doc.rero.ch

$$\eta_\alpha C_\alpha(i\hbar\nu) - \sum_\beta \Lambda_{\alpha\beta}(i\hbar\nu) C_\beta(i\hbar\nu) = \Phi_{\alpha 0}(i\hbar\nu), \quad \text{(A6)}$$

$$\alpha,\beta = 0,1,2,3$$

with $\eta_\alpha = +1(\alpha = 0,3)$ and $\eta_\alpha = -1(\alpha = 1,2)$. The coefficients of the system are given by

$$\sum_\alpha \tau_\alpha \Phi_{\alpha\beta} = \lambda \frac{k_B T}{N} \sum_{\boldsymbol{k},iE} w_{\boldsymbol{k}} t_{\perp\boldsymbol{k}} [\mathcal{G}_B(\boldsymbol{k},iE)\tau_\beta \mathcal{G}_A(\boldsymbol{k},iE + i\hbar\nu) - \mathcal{G}_A(\boldsymbol{k},iE)\tau_\beta \mathcal{G}_B(\boldsymbol{k},iE + i\hbar\nu)] \quad \text{(A7)}$$

and

$$\sum_\alpha \tau_\alpha \Lambda_{\alpha\beta} = \lambda \frac{k_B T}{N} \sum_{\boldsymbol{k},iE} w_{\boldsymbol{k}}^2 [\mathcal{G}_B(\boldsymbol{k},iE)\tau_\beta \mathcal{G}_A(\boldsymbol{k},iE + i\hbar\nu) + \mathcal{G}_A(\boldsymbol{k},iE)\tau_\beta \mathcal{G}_B(\boldsymbol{k},iE + i\hbar\nu)]. \quad \text{(A8)}$$

Finally, to get the response function, we insert the renormalized vertices into Eq. (23) and with the help of Tr $\tau_\alpha = 2\delta_{\alpha 0}$ obtain

$$\Pi_{\text{bl-bl}}^{\text{VC}} = \Pi_{\text{bl-bl}}^{\text{NV}} - \frac{2e^2 d_{\text{bl}}}{\hbar^2 a^2} \sum_\beta \Phi_{0\beta} C_\beta. \quad \text{(A9)}$$

All the above equations can be analytically continued to the real axis explicitly. For each frequency required, we have to evaluate the coefficients $\Phi_{\alpha\beta}$ and $\Lambda_{\alpha\beta}$, solve linear system (A6) and find response function (A9). Thanks to the simple form of the self-energy, the Matsubara summations can be again performed analytically, as in Eq. (A3), but lead to more cumbersome expressions due to the additional τ_β matrix in Eqs. (A7) and (A8).

http://doc.rero.ch

*chaloupka@physics.muni.cz

[1] C. C. Homes, T. Timusk, R. Liang, D. A. Bonn, and W. N. Hardy, Physica C **254**, 265 (1995).
[2] J. Schutzmann, S. Tajima, S. Miyamoto, Y. Sato, and R. Hauff, Phys. Rev. B **52**, 13665 (1995).
[3] C. Bernhard, D. Munzar, A. Wittlin, W. König, A. Golnik, C. T. Lin, M. Kläser, Th. Wolf, G. Müller-Vogt, and M. Cardona, Phys. Rev. B **59**, R6631 (1999).
[4] K. Tamasaku, Y. Nakamura, and S. Uchida, Phys. Rev. Lett. **69**, 1455 (1992).
[5] C. C. Homes, T. Timusk, R. Liang, D. A. Bonn, and W. N. Hardy, Phys. Rev. Lett. **71**, 1645 (1993).
[6] D. N. Basov and T. Timusk, Rev. Mod. Phys. **77**, 721 (2005).
[7] S. Chakravarty, H. Y. Kee, and K. Volker, Nature (London) **428**, 53 (2004).
[8] D. Munzar, T. Holden, and C. Bernhard, Phys. Rev. B **67**, 020501(R) (2003).
[9] O. K. Andersen, A. I. Liechtenstein, O. Jepsen, and F. Paulsen, J. Phys. Chem. Solids **56**, 1573 (1995).
[10] I. I. Mazin, S. N. Rashkeev, A. I. Liechtenstein, and O. K. Andersen, Phys. Rev. B **46**, 11232 (1992).
[11] D. Munzar, C. Bernhard, A. Golnik, J. Humlíček, and M. Cardona, Solid State Commun. **112**, 365 (1999).
[12] M. Grüninger, D. van der Marel, A. A. Tsvetkov, and A. Erb, Phys. Rev. Lett. **84**, 1575 (2000).
[13] D. van der Marel and A. Tsvetkov, Czech. J. Phys. **46**, 3165 (1996).
[14] N. Shah and A. J. Millis, Phys. Rev. B **65**, 024506 (2001).
[15] S. V. Borisenko, A. A. Kordyuk, V. Zabolotnyy, J. Geck, D. Inosov, A. Koitzsch, J. Fink, M. Knupfer, B. Büchner, V. Hinkov, C. T. Lin, B. Keimer, T. Wolf, S. G. Chiuzbăian, L. Patthey, and R. Follath, Phys. Rev. Lett. **96**, 117004 (2006).
[16] D. L. Feng, N. P. Armitage, D. H. Lu, A. Damascelli, J. P. Hu, P. Bogdanov, A. Lanzara, F. Ronning, K. M. Shen, H. Eisaki, C. Kim, J.-i. Shimoyama, K. Kishio, and Z.-X. Shen, Phys. Rev. Lett. **86**, 5550 (2001).
[17] Y. D. Chuang, A. D. Gromko, A. Fedorov, Y. Aiura, K. Oka, Yoichi Ando, H. Eisaki, S. I. Uchida, and D. S. Dessau, Phys. Rev. Lett. **87**, 117002 (2001).
[18] A. A. Kordyuk, S. V. Borisenko, T. K. Kim, K. A. Nenkov, M. Knupfer, J. Fink, M. S. Golden, H. Berger, and R. Follath, Phys. Rev. Lett. **89**, 077003 (2002).
[19] S. V. Borisenko, A. A. Kordyuk, T. K. Kim, S. Legner, K. A. Nenkov, M. Knupfer, M. S. Golden, J. Fink, H. Berger, and R. Follath, Phys. Rev. B **66**, 140509(R) (2002).
[20] Li Yu, D. Munzar, A. V. Boris, P. Yordanov, J. Chaloupka, T. Wolf, C. T. Lin, B. Keimer, and C. Bernhard, Phys. Rev. Lett. **100**, 177004 (2008).
[21] S. V. Dordevic, E. J. Singley, J. H. Kim, M. B. Maple, Seiki Komiya, S. Ono, Yoichi Ando, T. Rõõm, Ruxing Liang, D. A. Bonn, W. N. Hardy, J. P. Carbotte, C. C. Homes, M. Strongin, and D. N. Basov, Phys. Rev. B **69**, 094511 (2004).
[22] J. Chaloupka and D. Munzar, Phys. Rev. B **76**, 214502 (2007).
[23] A. I. Liechtenstein, O. Gunnarsson, O. K. Andersen, and R. M. Martin, Phys. Rev. B **54**, 12505 (1996).
[24] M. Eschrig and M. R. Norman, Phys. Rev. Lett. **89**, 277005 (2002).
[25] M. Eschrig and M. R. Norman, Phys. Rev. B **67**, 144503 (2003).
[26] M. Eschrig, Adv. Phys. **55**, 47 (2006).
[27] D. J. Scalapino, S. R. White, and S. C. Zhang, Phys. Rev. Lett. **68**, 2830 (1992).
[28] R. Peierls, Z. Phys. **80**, 763 (1933).
[29] J. M. Luttinger, Phys. Rev. **84**, 814 (1951).
[30] Y. Nambu, Phys. Rev. **117**, 648 (1960).
[31] J. R. Schrieffer, *Theory of Superconductivity* (Addison-Wesley, Reading, MA, 1988).
[32] P. Cásek, C. Bernhard, J. Humlíček, and D. Munzar, Phys. Rev. B **72**, 134526 (2005).
[33] H. J. Vidberg and J. W. Serene, J. Low Temp. Phys. **29**, 179 (1977).
[34] D. E. Aspnes, Am. J. Phys. **50**, 704 (1982).
[35] H. Ehrenreich, in *The Optical Properties of Solids*, edited by J.

Tauc (Academic Press, New York, 1966), Vol. 34.
[36] N. N. Bogoljubov, V. V. Tolmachov, and D. V. Širkov, Fortschr. Phys. **6**, 605 (1958).
[37] P. W. Anderson, Phys. Rev. **110**, 827 (1958).
[38] M. Tinkham, *Introduction to Superconductivity* (McGraw-Hill, New York, 1996).
[39] C. Bernhard, Li Yu, A. Dubroka, K. W. Kim, M. Rössle, D. Munzar, J. Chaloupka, C. T. Lin, and Th. Wolf, J. Phys. Chem. Solids **69**, 3064 (2008).
[40] V. Železný, S. Tajima, D. Munzar, T. Motohashi, J. Shimoyama, and K. Kishio, Phys. Rev. B **63**, 060502(R) (2001).
[41] D. Munzar, C. Bernhard, T. Holden, A. Golnik, J. Humlíček, and M. Cardona, Phys. Rev. B **64**, 024523 (2001).
[42] C. Bernhard, T. Holden, A. Golnik, C. T. Lin, and M. Cardona, Phys. Rev. B **62**, 9138 (2000).
[43] M. Mori, T. Tohyama, and S. Maekawa, J. Phys. Soc. Jpn. **75**, 034708 (2006).
[44] M. Mori, T. Tohyama, and S. Maekawa, Phys. Rev. B **66**, 064502 (2002).
[45] W. S. Lee, I. M. Vishik, K. Tanaka, D. H. Lu, T. Sasagawa, N. Nagaosa, T. P. Devereaux, Z. Hussain, and Z.-X. Shen, Nature (London) **450**, 81 (2007).
[46] K. Tanaka, W. S. Lee, D. H. Lu, A. Fujimori, T. Fujii, Risdiana, I. Terasaki, D. J. Scalapino, T. P. Devereaux, Z. Hussain, and Z.-X. Shen, Science **314**, 1910 (2006).
[47] A. B. Kuzmenko, N. Tombros, H. J. A. Molegraaf, M. Grüninger, D. van der Marel, and S. Uchida, Phys. Rev. Lett. **91**, 037004 (2003).
[48] D. N. Basov, S. I. Woods, A. S. Katz, E. J. Singley, R. C. Dynes, M. Xu, D. G. Hinks, C. C. Homes, and M. Strongin, Science **283**, 49 (1999).
[49] M. R. Norman, M. Randeria, B. Janko, and J. C. Campuzano, Phys. Rev. B **61**, 14742 (2000).

http://doc.rero.ch